616

PROPOSAL TO MEASURE NEUTRINO STRUCTURE FUNCTIONS

(Including $R = \sigma_L/\sigma_T$)

2755-PH 1709-GS 902-GS 2684-PH 936-PH 94-PH

CIT R. Blair, J. Lee, P. Linsay, J. Ludwig, R. Messner, F. Sciulli and M. Shaevitz 431-PH

California Institute of Technology, Pasadena, California 91125

364-MA 1342-PH 2542-PH 727-PH 1389-PH 754-PH

J. F. Bartlett, E. Fisk, Y. Fukushima, Q. Kerns, T. Kondo, S. Segler, R. Stefanski, 466-PH D. Theriot, 156-PH and D. Yovanovitch 85-PH

FNAL Fermi National Accelerator Lab, Batavia, Illinois 60510

1750-PH 1687-PH 2578-PH

A. Bodek, R. Coleman, and W. Marsh

ROC University of Rochester, Rochester, New York 14627

283-PH 1087-PH

O. Fackler and K. Jenkins

ROK Rockefeller University, New York, N.Y. 10021

January, 1979

Spokesman: F. Sciulli
Caltech

Contents

	Page
Abstract	1
I. Introduction	3
A. The Structure Functions	3
B. F_1, F_3 and Test of Charge Symmetry	4
C. Measurement of $R = \sigma_L/\sigma_T$	6
II. Technique for Extracting R	9
A. Form of Fitted Equations	9
B. Appearance of Data with Finite R	11
III. Available Energy Range and Event Rates	13
A. Neutrino Energy Ranges	13
B. Event Rates for ν_μ and $\bar{\nu}_\mu$: A Specific Set of Runs	15
IV. Statistical Accuracy	17
A. Fits to $(\sigma + \bar{\sigma})$ to Obtain R and F_1 at Fixed x, q^2	19
B. Fits to $(\sigma - \bar{\sigma})$ to Obtain F_3 and G_3 at Fixed x, q^2	21
V. Requirements on the Precision of Energy and Flux Measurements	23
A. Neutrino Flux	23
B. Systematic Errors on Energy Measurement	23
VI. Resolutions and Other Corrections - General	24
VII. Effect of Resolution on R and f_1	25
VIII. Radiative Corrections	31
IX. Charge Symmetry Effects that Influence y-distributions	36
X. Needs and Requirements	39
XI. References	43
Appendices:	
A. Flux Monitoring System	44
B. Lab E Apparatus	57
C. Position Detection	66
D. Calorimetry	72
E. Comparison of this Experiment with its European Counterpart	82

List of Figures: Page

Figure 1:	Theoretical predictions for $R = \sigma_L/\sigma_T$	7
Figure 2:	Polarization of virtual boson propagator	10
Figure 3:	Representation of the data according to Equation 9	12
Figure 4:	Sketch of Dichromatic Beam Geometry	13
Figure 5:	Neutrino Energies at Lab E	14
Figure 6:	Events per GeV of neutrino energy as a function of dichromatic beam energy settling	16
Figure 7:	Statistical standard deviations expected for data of Table III in regions of x and q^2 for simultaneous fits to R and f	20
Figure 8:	Statistical standard deviations expected for data in Table III for f_3 and g_3	22
Figure 9:	Error matrix parameters	26
Figure 10:	Errors on $x(\sigma_x)$ vs. y parameter for various x-values	27
Figure 11:	Fitted R and f, values for data uncorrected for resolutions	29
Figure 12:	Calculated effect of radiative corrections on $\tau(y)$ due to term proportional to neutrino to neutrino energy	35
Figure 13:	Calculated effects of charge symmetry deviations with $g_1/f_1 = 0.094$	38
Figure A1:	Neutrino Beam Line for E356	45
Figure A2:	Expansion port instrumentation	46
Figure A3:	Linearity of Ion Chamber response	49
Figure A4:	ν_π Event vertex distribution in the detector	51
Figure A5:	Cerenkov curve at +200 GeV	53
Figure A6:	Positive K/π ratio	55
Figure A7:	Positive P/π ratio	56
Figure B1:	Lab E apparatus	58
Figure B2:	Target Cart Arrangement	59
Figure B3:	Tri-muon event	61
Figure B4:	Toroid arrangement	62

List of Figures (cont.) Page

Figure C1: Experimental determination of spark presence on muon tracks near interaction vertex 67

Figure C2: Projected angle error vs. muon energy 68

Figure C3: Typical event 69

Figure C4: Fractional error for momentum measurement vs. momentum 71

Figure D1: Pulse height distribution for muons traversing the center of a counter 73

Figure D2: Pulse height distribution for 100 GeV hadrons in the center of a target cart 74

Figure D3: Linearity curve: Pulse height versus hadron shower energy 76

Figure D4: Energy resolution for hadron showers 77

Figure D5: Variation of pulse height with position 78

Figure D6: Mean observed total neutrino energy vs. radius in detector 80

Figure E1: Typical acceptance at fixed x values for CFRR apparatus 84

Figure E2: CDHS acceptance 85

Figure E3: Angular resolution with two different approaches to position detection 88

List of Tables

Table I: Estimated Apparent Charge Symmetry Violations Due to a n/p Excess 5

Table II: Previous Measurements of R 6

Table III: Possible Scenario of Running 17

Table IV: Example of subset of data $0.1 < 0.4$ and $37.5 < E_h <$ 62.5 GeV 18

Table V: Apparent Values of R and f_i obtained due to resolution effects and applying no correction 30

Table VI: Characteristic Values in the radiative correction difference on neutrinos and anti-neutrinos 33

Table VII: Estimate of relative size of charge symmetry deviation effects 36

Table VIII: Monitor Requirements 41

Table E1: Comparison of this experimental apparatus with its European counterpart 83

Abstract

We propose to make a definitive measurement of the three charged current structure functions: $F_2(x,q^2)$, $2xF_1(x,q^2)$, and $xF_3(x,q^2)$. These measurements will cover a significant range of x and q^2 with neutrino energies between 25 and 250 GeV (see Section III). Of particular importance and special emphasis is the measurement of $F_L = F_2 - 2xF_1$, or $R \equiv F_L/2xF_1$, which was predicted to be very near zero in the naive parton model, but is expected to be measurable finite ($R \gtrsim 0.12$) in quantum chromodynamic theories. Existing older measurements of this parameter in νp and ep, while large enough on average for QCD, do not show the x-dependence expected. A newer measurement with small quoted error appears inconsistent with QCD.

The structure functions will be extracted (see Section III) from (a) the difference of the ν_μ and $\bar{\nu}_\mu$ cross sections (xF_3), and (b) the sum of the ν_μ and $\bar{\nu}_\mu$ cross sections (F_2 and F_L). The extraction of R (F_L) and F_2 from the sum of the cross sections requires fits to a y-distribution at fixed x,q^2. Experiments to date (see Section Ia) have not had the statistical power to make this two-parameter fit, and so their results on F_3 have depended on assumptions made for R. This would be the first experiment capable of the statistical power to measure R and F_2 with sufficient precision. We expect 12 separate bins of x and q^2 with statistical precision on R ranging from .04 to .10 (see Section IV).

Investigation into the systematic problems inherent in this measurement (see Sections V-IX) reassures us that systematic effects can be controlled to the level necessary to make such errors small in comparison to the statistical errors. The largest likely distortion is likely to come from the finite resolutions in angle and energy. With no correction, the induced R would be of the order the statistical error, or less (.04 to .09). Distortions due to higher-order radiative processes and known charge-symmetry violations (e.g., production from strange sea) are smaller. We believe the precision of the result will be primarily governed by the statistical level of the proposed experiment.

I. Introduction

A. The structure functions

A very significant and important problem largely unique to neutrino physics at the highest present energies is the extraction of the three structure functions (F_2, xF_3, and F_L) which describe the nucleon's structure in terms of point-like constituents and the interactions between those constituents. Recent theoretical developments (QCD) make definitive predictions about these structure functions. Although there have been qualitative corroborations[1,2] of some of the features of these theoretical approaches, clear and definitive verifications do not yet exist. Also, some contrary evidence[8] has recently been presented (see section C). In this confused situation, precise measurements of structure functions will provide both strong tests of existing theory as well as a challenge to future theory to relate the structure functions to each other and to other data. They are likely to be the anchor-point for studies, at super-high energies, of pp or $\bar{p}p$ interactions, and absolutely essential to attempts to find propogator damping of the neutrino cross-section at Tevatron energies.

At high q^2, the general form of the neutrino scattering cross-section (per nucleon) assuming V-A, an isoscalar target and charge symmetry, may be written ($q^2 >> M^2$, M = nucleon mass):

$$\frac{d(\sigma-\bar{\sigma})}{dx\ dy} = \frac{G^2ME}{\pi} f_3(x,q^2) \left\{1-(1-y)^2\right\} \tag{1}$$

$$\frac{d(\sigma+\bar{\sigma})}{dx\ dy} = \frac{G^2ME}{\pi} \left[\left\{1+(1-y)^2\right\} f_1(x,q^2) + 2(1-y) f_L(x,q^2)\right] \tag{2}$$

where $\quad f_L(x,q^2) = Rf_1(x,q^2) = \frac{R}{1+R} f_2(x,q^2)$

In the more common notation,

$$f_2(x,q^2) = F_2(x,q^2)$$

$$f_1(x,q^2) = 2xF_1(x,q^2)$$

$$f_3(x,q^2) = xF_3(x,q^2)$$

In the notation familiar to electron scattering

$$R \equiv \sigma_L/\sigma_T$$

is the ratio of longitudinal (transversely aligned boson propagator) to transverse (longitudinally aligned boson propagator) cross-sections. Here, as usual, $y = E_h/E$, $x = q^2/2ME_h$, $q^2 = EE'\theta^2$.

From the purely phenomenological point-of-view, it is extremely important to measure R. All measurements of structure functions [i.e. $F_2(x,q^2)$] to the present have made some assumption, either explicitly or implicitly, regarding R. If, as is consistent with most of the present data, R is significantly non-zero, "measurements" of f_1 and f_2 may require dramatic modifications.

B. f_1 and f_3 and test of charge symmetry

Clearly, it is of importance to measure all three of these structure functions well. $f_1(x,q^2)$ is usually thought to be related to the sum of all quark and anti-quark components of the nucleon. $f_3(x,q^2)$ is the parity-violating structure function, related to the difference between quark and anti-quark components. As such, there are particularly simple predictions[3] for its q^2 behavior in the context of QCD. Both structure functions are expected to be directly related to the analogous structure functions in μ or e scattering.

It is the intention of this experiment to make precise measurements of all of these structure functions in order to make comparisons with prediction. However, this proposal will make its primary emphasis on measuring f_L, or R, very well, for reasons which will be explained later (see section I.C.).

One important feature of high statistics measurements will be a definitive test of charge symmetry. The energy range of this experiment lies dominantly well above charm threshold. Taking into account the expected quark constituents, the more precise form for equation (1) is

$$\frac{d(\sigma-\bar{\sigma})}{dx\,dy} = \frac{G^2ME}{\pi}\left\{f_3(x,q^2)[1-(1-y)^2]+g_3(x,q^2)[1+(1-y)^2]\right\} \quad (1a)$$

where
$$f_3 = \frac{x}{2}\left[(u+d) - (\bar{u}+\bar{d}) + (s+c) - (\bar{s}+\bar{c})\right]$$
$$g_3 = \frac{x}{2}\left[\delta(u-d) - \delta(\bar{u}-\bar{d}) + (s-c) - (\bar{s}-\bar{c})\right]$$

Here, for example, $xu(x) \equiv xu_p(x)$ = distribution of u quarks in proton and we have assumed

$$xu_p(x) = xd_n(x) \quad \text{etc.}$$

$$\delta = \frac{N-Z}{A} = \text{neutron excess (.07 for Fe)}$$

Table I gives the expected ratio g_3/f_3 due to neutron-proton excess and u/d asymmetry from phenomenological fits at representative x-values.

x	g_3/f_3
.06	.008
.21	.023
.61	.032

Table I: Estimated apparent charge symmetry violations due to a n/p excess.

Production from u, d, s, c and their antiparticles in a charge asymmetric way (e.g. new quark production) should be visible at these levels. The statistical accuracy of the tests will be discussed later. It should be noted that present tests of charge symmetry[4] are in the 5-10% range, and exist only at y=0, where new quark production would not be visible.

C. Measurement of $R = \sigma_L/\sigma_T$

The emphasis of our effort in preparing this document has been to determine both how and how well the R-parameter might be measured. This by no means indicates de-emphasis of the effort in making good measurements of all structure functions. We concentrate on the R-measurement because

(1) Measurements of R are by far the most difficult. In carrying out the experiment and the analysis, values of f_1 and f_3 are almost automatic by-products at the same x, q^2 values.

(2) Present knowledge of R is abysmal, whereas some measurements of f_1 and f_3 have been tentatively made.

(3) There are very well-defined predictions for the behaviour of R in QCD, which we discuss in this section

We summarize knowledge of R from all forms of lepton-nucleon scattering below in table II.

Table II: Previous Measurements of R

Technique	x-range	Q^2 range	Value of R
ep scattering[5]	0.1-0.9	2-20 GeV^2	0.2 ± 0.1
μp scattering[6]	0 - 0.1	1-12.5 GeV^2	$0.44 \pm 0.25 \pm 0.19$
νp scattering[7]	0-1.	0.1-50 GeV^2	$0.15 \pm 0.10 \pm 0.04$
νp scattering[8]	0-1.	2-200 GeV^2	-0.03 ± 0.04
νp scattering[12]	0-1	2-200 GeV^2	$0.18 \pm 0.06 \pm 0.04$

Although most of these indicate a non-zero value for R, little more can be said, except perhaps, in the words of one group[5], "There is no evidence for a fall-off of R with q^2 or x'." The most recent value[8], very close to $R \approx 0$, uses an analysis technique that is controversial, and is very different from the others in table II.

These results should be contrasted with the theoretical predictions shown in Fig. 1 below.[9] It should be noted that a typical value of R is finite (e.g. $R \approx 0.12$ at $q^2 = 20$ GeV^2 averaged over x) in these calculations, and falls roughly as $1/\ln q^2$.

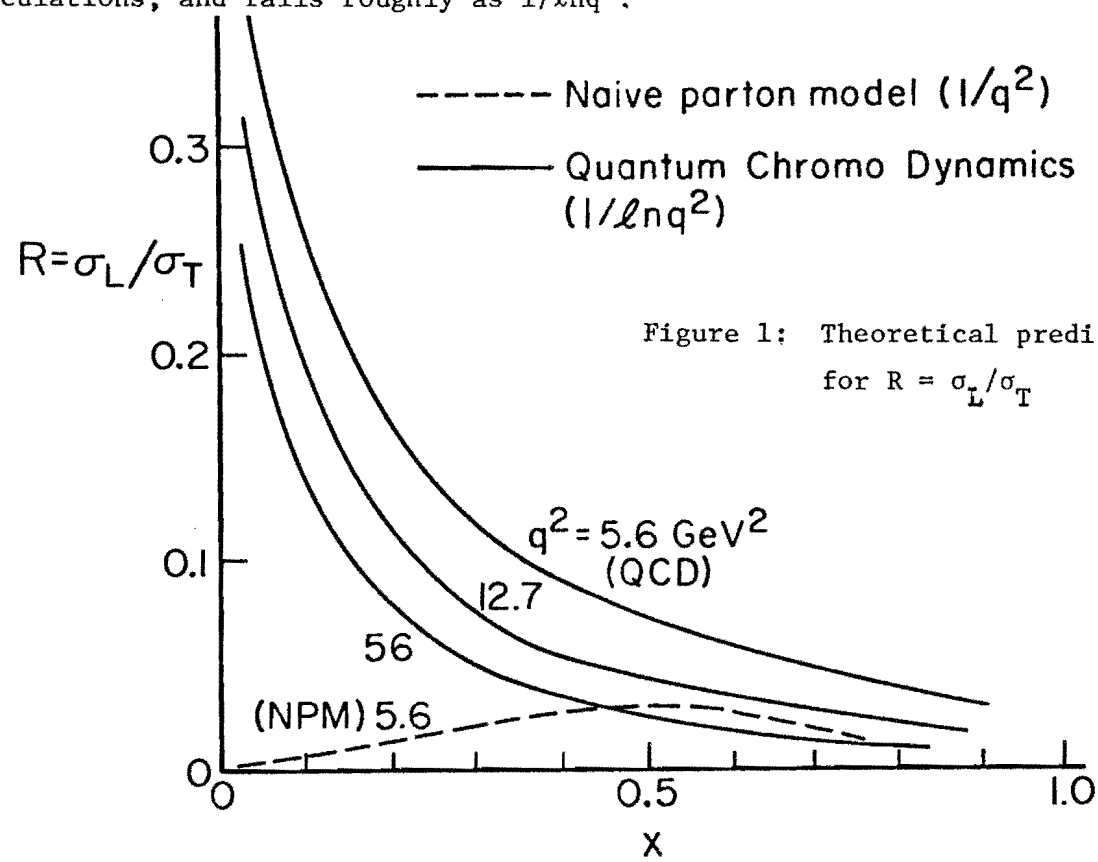

Figure 1: Theoretical predictions for $R = \sigma_L/\sigma_T$

A measurement of R is usually touted as a test of the Callan-Gross relation, or in more physical terms, a test of spin 1/2 carried by the nucleon constituents. Finite values of R can be <u>induced</u> with spin 1/2, if the neutrino interacts with a constituent carrying finite momentum transverse to the direction of motion ($P_\perp$). In the naive parton model, R may be thought of as originating from an intrinsic $P_\perp = k_o$ of the constituents inside the nucleon, in which case

$$R_{NPM} \propto \frac{4k_o^2}{q^2}$$

and should fall dramatically with q^2, and to be so small as to be unmeasurable for $q^2 >> 1$ GeV^2. In QCD, the quark $P_\perp$ is predicted to rise with q^2 ($P_\perp^2 \simeq \beta(x,q^2)q^2$) due to exchange of virtual gluons. However, the coupling to the gluons in $\beta(x,q^2)$ should fall like $1/\ln(q^2/\Lambda^2)$.

In that case

$$R_{QCD} \propto \frac{\alpha(x)q^2}{q^2} \frac{1}{\ln q^2} \approx \frac{\alpha(x)}{\ln q^2}$$

where $\alpha(x)$ is some function of x. Specifically, the value of the longitudinal structure function is given by

$$f_L^{QCD}(x,q^2) = \frac{\alpha_s(q^2)}{2\pi} x^2 \left[\int_x^1 \frac{dz}{z^3} \frac{8}{3} F_2(z,q^2)dz + \int_x^1 \frac{dz}{z^3} 16(1-\frac{x}{z}) G(z,q^2)dz \right]$$

where $F_2(z)$ and $G(z)$ are z times the distributions in fractional momentum z, carried by the quarks and gluons, respectively. The coefficient is the quark-gluon coupling constant, $\alpha_s(q^2) = 12\pi/(33-2n)\ln^{-1}q^2/\Lambda^2$. The integrals make it likely that $f_L(x,q^2)$ will be strongly peaked at small x.

Interestingly, the average value, $\bar{R}(q^2) \equiv \int f_L(x,q^2)\,dx/\int f_2(x,q^2)dx$, has a rather well-defined prediction

$$\bar{R}(q^2) = \frac{\alpha_s(q^2)}{2\pi} \left[\frac{8}{9} + \frac{4}{3} \int_o^1 G(x,q^2)dx/\int_o^1 F_2(x,q^2)dx \right]$$

where the ratio in the last term is just the ratio of momentum carried by quarks and gluons, usually taken to be about unity. This approach predicts that $\bar{R}(20\text{ GeV}^2) \approx 0.12$, strongly peaked at small x and very small at large x.

Interestingly, of the data referred to in table II, ref. 5 does not have this qualitative behavior, although the value of R is large. If R is large at large x and large q^2, that fact could not easily be accommodated in any model with spin 1/2 constituents. Conversely, the result with the smallest quoted error, ref. 8, is inconsistent with the QCD estimate.

The problem of R is an important and unsettled one. In this context there are three crucial and unanswered questions:

1) Is the value of R large at small x?

2) Is the value of R small at large x?

3) Is the q^2 dependence of R like $1/q^2$ or like $1/\ell nq^2$ or like neither of these?

II. Technique for Extracting R

A. Form of fitted equations

Pedagogically, the formulae for R from electron scattering experiments[5] are very attractive:

$$\frac{d^2\sigma}{d\Omega' dE'} = \frac{4\alpha^2}{q^4} \frac{E'^2}{\nu} \cos^2 \frac{\theta}{2} f_2^{ep}(x,q^2) \frac{1+\varepsilon R^{ep}(x,q^2)}{1+R^{ep}(x,q^2)} \tag{3}$$

$$\varepsilon = \frac{1}{1+2\tan^2\frac{\theta}{2}(1+\frac{\nu^2}{Q^2})} \tag{4}$$

where ε is the polarization of the exchanged virtual photon. Sensitivity to R is, to a large extent, determined by the range of ε which can be covered. For $q^2 << E^2$, these can be rewritten

$$\frac{d\sigma}{dx\, dy} = \frac{8\pi\alpha^2}{q^4} ME f_2^{ep}(x,q^2) \frac{1-y}{\varepsilon} \frac{1+\varepsilon R^{ep}(x,q^2)}{1+R^{ep}(x,q^2)} \tag{5}$$

$$\varepsilon = \frac{2(1-y)}{1+(1-y)^2} \tag{6}$$

The sum of neutrino and anti-neutrino cross-sections follows with the trivial substitutions $8\pi\alpha^2/q^4 \to G^2/\pi$, $f_2^{ep} \to f_2$; $R^{ep} \to R$:

$$\frac{d(\sigma+\bar{\sigma})}{dx\ dy} = \frac{G^2ME}{\pi} f_2(x,q^2) \frac{1-y}{\varepsilon} \frac{1+\varepsilon R(x,q^2)}{1+R(x,q^2)} \tag{7}$$

with ε still given by equation (6). This is formally equivalent to equation (2).

That is,

$$\frac{d(\sigma+\bar{\sigma})}{dx\ dy} = \frac{G^2ME}{\pi} f_1(x,q^2)[1+(1-y)^2][1+\varepsilon(y)R(x,q^2)] \tag{8}$$

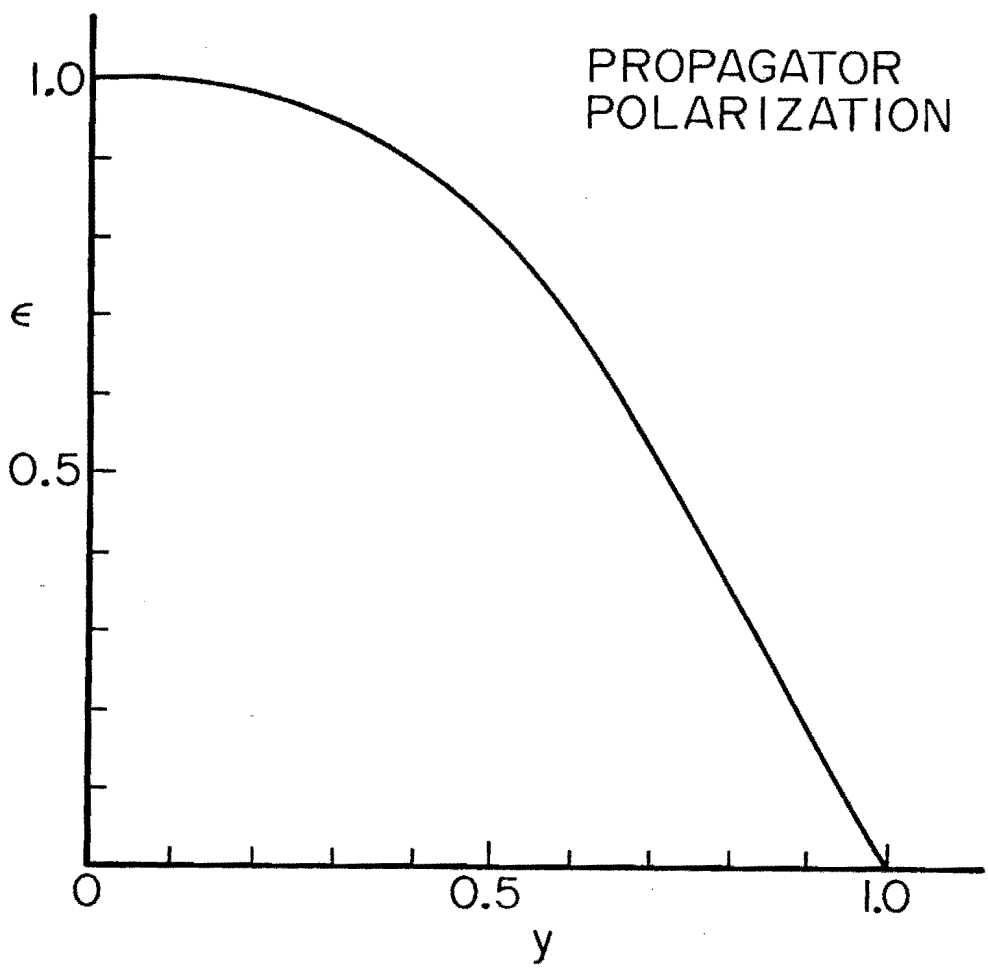

Figure 2: Polarization of virtual boson propagator versus y = fraction of neutrino energy carried by the propagator.

The virtual boson polarization versus y (eq. 6), is shown in figure 2. As a specific example of the range of ε available, consider the following choice: $x = 0.33$, fixed $E_h = 100$ GeV (i.e. $q^2 \simeq 67$ GeV^2) $100 < E < 250$ GeV, so that $.4 < y < 1$ and $0 < \varepsilon < .90$.

One very important point should be made in regard to equation (8), which also helps to explain the specific example chosen above. Since both $f_1(x,q^2)$ and $R(x,q^2)$ are expected to depend on both x and q^2, it is of fundamental importance to plot y-distributions for <u>both</u> x <u>and</u> q^2 fixed. One can always accommodate fixed x <u>or</u> q^2 by making specific angle and energy cuts. But, since $q^2=2ME_hx$, to fix <u>both</u> x <u>and</u> q^2 simultaneously, the y distribution must be made with E_h fixed. (The alternative would be to extrapolate the data according to some theoretical predisposition; this approach should be avoided at all costs). Since $y = E_h/E$, y distributions must be made with fixed E_h and variable E. Hence, data must be taken over a wide range of neutrino energies. The accessible x and q^2 bins in the context of the energies for this experiment will be discussed later.

B. Appearance of data with finite R.

Rewriting equation (8),

$$\tau(y) = \frac{\pi}{G^2ME} \frac{1}{[1+(1-y)^2]} \frac{d(\sigma+\bar{\sigma})}{dx\ dy} = f_1(1+\varepsilon(y)R) \qquad (9)$$

where the data, and hence f_1 and R are understood to be at fixed x and q^2.

If nature produces finite R, the quantity $\tau(y)$ will show behavior characteristic of the dashed curve in figure 3, with intercept at y=0 relative to y=1 having

$$\frac{\tau(y=0) - \tau(y=1)}{\tau(y=1)} = R \qquad (10)$$

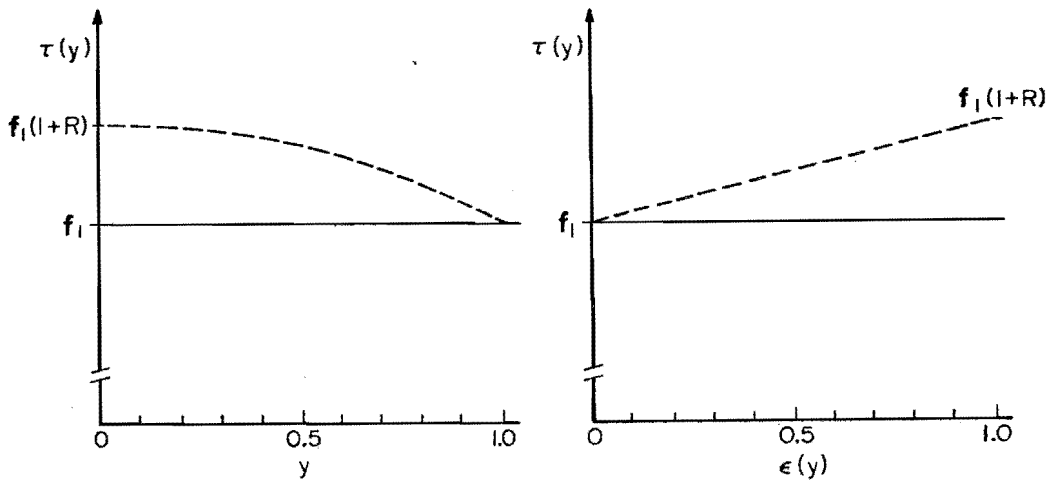

Figure 3a

Figure 3b

Figure 3: (a) Representation of the data according to equation (9), with $R = 0$ (solid line) and finite R (dashed line) τ vs. y. (b) Same as figure 3(a), but $\tau(y)$ plotted vs. $\varepsilon(y)$.

In summary, therefore, a very crucial element must be present in the analysis: y-distributions must be made at fixed final state hadron energy, E_h, in order to ensure both q^2 and x fixed. A wide range of neutrino energies must be covered to vary $y = E_h/E$ at fixed E_h. The effects of systematic problems in extracting R will be addressed later.

III. Available Energy Range and Event Rates

In order to cover as complete a range of ε (see Section II), or y, at fixed E_h, a broad range of neutrino energies is desirable. The dichromatic beam will be used to produce the neutrinos for this experiment, in order to minimize systematic errors and provide flux normalization.

A. Range of Neutrino (Antineutrino) Energies

The neutrino energy for a monochromatic (π,K) beam at energy E_o directed at the center of the detector is given by

$$E = \frac{E_o(1-m_\mu/m_{\pi,K})^2}{1 + (r/r_o)^2} \tag{11}$$

where r is the radius at the detector, and $r_o = D/\gamma$ (see Fig. 4) and $\gamma = E_o/m_{\pi,k}$.

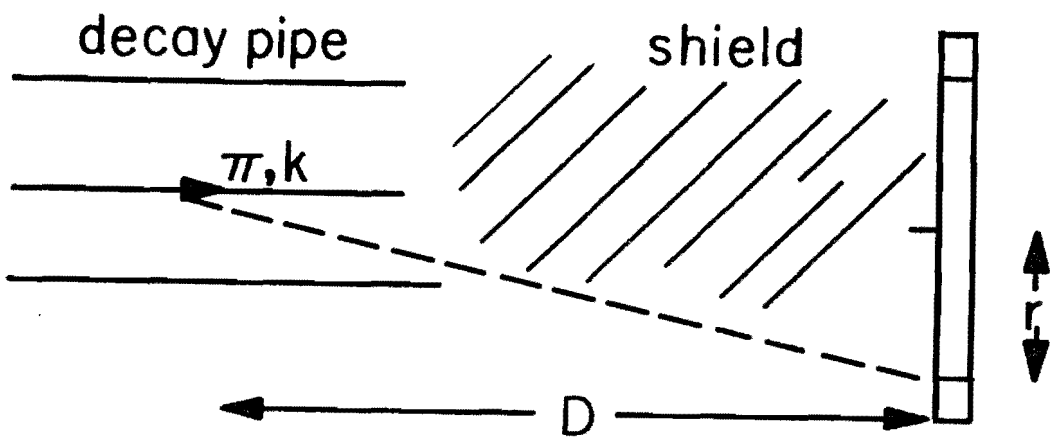

Figure 4: Sketch of dichromatic beam geometry. At Lab E, D ≈ 950 m.

Both pion and kaon neutrinos will be used to cover the entire energy range.

Figure 5 shows the range of neutrino energies available at the lab E detector as a function of beam energy setting, E_o. The solid curves show the neutrino energy at the center (r=0) of the target, and the dashed curves give the energy at a radius within the ten-foot square (r = 1.45m).

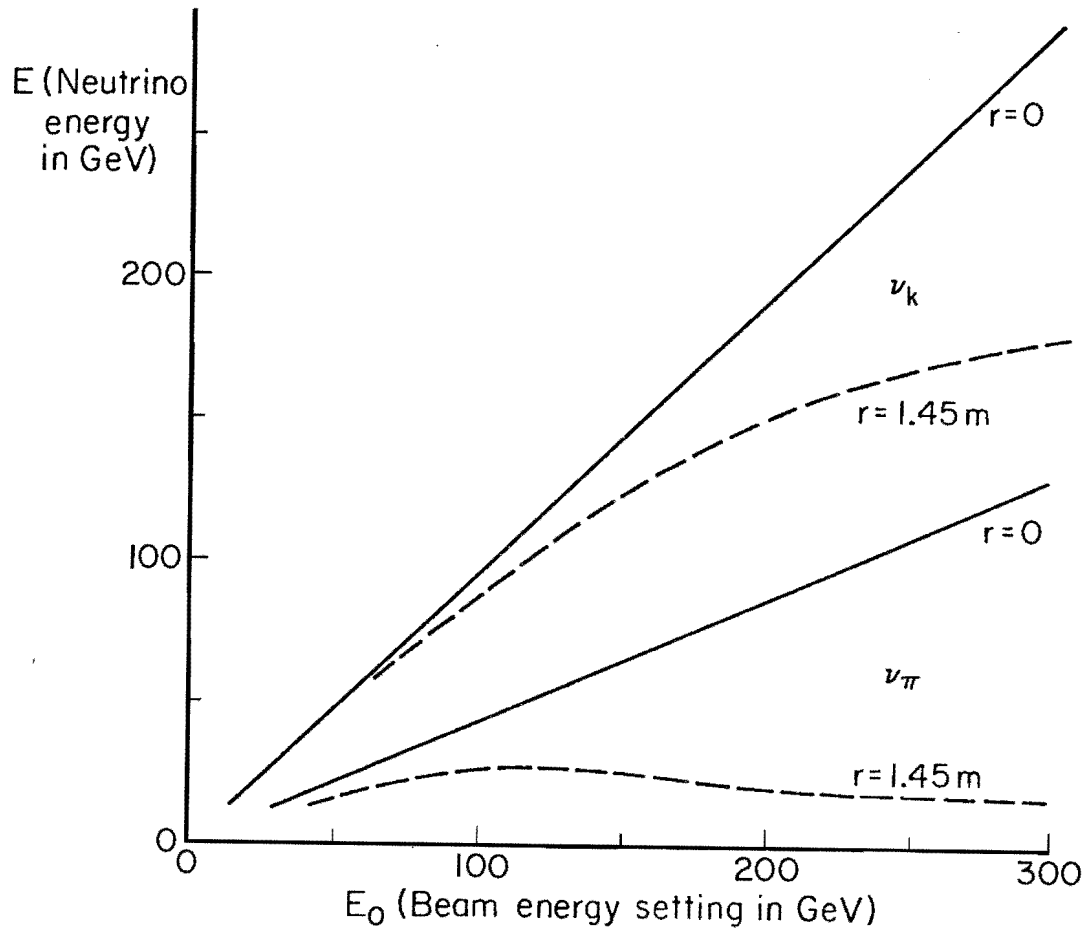

Figure 5

Figure 5: Neutrino energies at Lab E

Note that neutrino energies between 15 and 290 GeV are available for beam energy settings up to E_o = 300 GeV. A variety of settings are, however, necessary in order to span the entire range.

B. Event Rates for ν_μ and $\bar{\nu}_\mu$: A specific set of runs

Figure 6 shows the number of neutrino events per GeV of neutrino energy as a function of beam setting. Clearly, the antineutrino events are the most difficult to obtain in profusion. This is partially compensated by the fact that such events make a smaller contribution due to their smaller cross-section, especially at larger y where $\varepsilon(y)$ varies fastest. With 400 GeV protons, it is possible to explore energies with beam settings up to $E_o \approx 250$ GeV. With some antineutrino running at 450 GeV proton energy, this could be extended to $E_o \approx 300$ GeV.

We choose as a representative scenario the running shown in Table III in order to illustrate the statistical level of this experiment. This table has our experimental acceptance folded in and agrees with event rates obtained in E356. We would further optimize before running, however, preliminary investigations indicate that the statistical accuracy of the results will not be significantly improved by further optimization. The table assumes total running of 2×10^{19} protons with 400 GeV primary energy. At the higher energy points, a factor of 2 fewer 450 GeV protons would be required to achieve the same number of events.

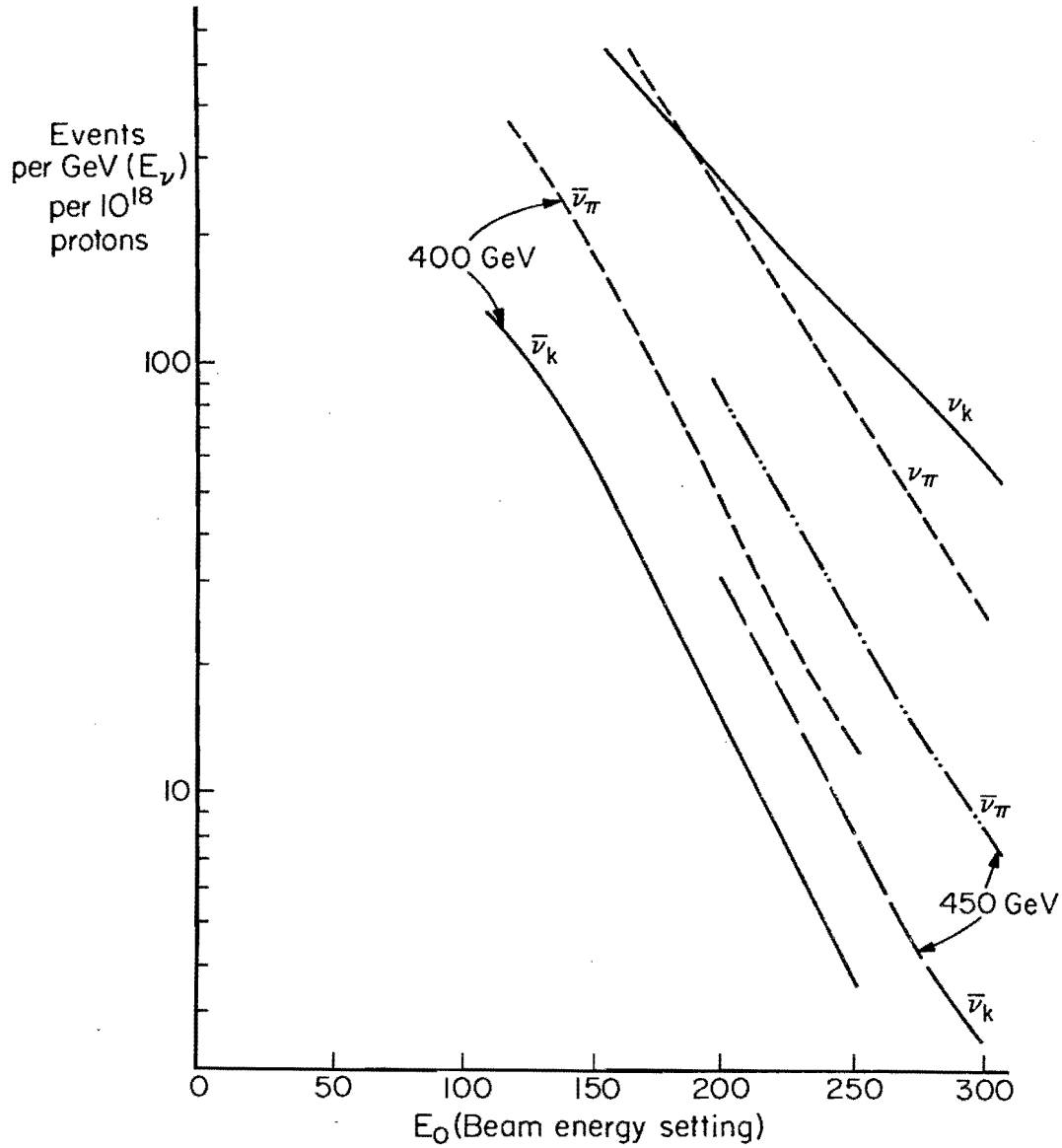

Figure 6

Figure 6: Events per GeV of neutrino energy as a function of dichromatic beam energy setting. All settings assume 400 GeV protons incident, except for higher energy antineutrino settings, where 450 GeV curves are labelled.

Table III: Possible Scenario of Running

Beam Setting	ν_K energy range	ν_π energy range	Positive running		Negative running	
			Protons	ν_π ν_K Events	Protons	$\bar{\nu}_\pi$ $\bar{\nu}_K$ Events
250 GeV	170-240 GeV	20-110	6.0×10^{18}	45000 51000	6.0×10^{18}	7500 1650
200 GeV	150-190 GeV	20-88	$2.\times10^{18}$	30000 21000	$2.\times10^{18}$	5900 1200
165 GeV	135-160 GeV	23-71	1.0	24000 11000	1.0	6500 1000
140 GeV	118-135 GeV	26-60	0.6	18000 6300	0.6	4500 690
120 GeV	105-115 GeV	27-51	0.4	18000 4000	0.4	3400 420
Total			1×10^{19}	135000 93800	1×10^{19}	27800 4960
				228300		32760
				—261000—		

IV. Statistical Accuracy

In the analysis of the hypothetical data of Table III, we assume that the data would be broken initially into three distinct x-bins in order to simultaneously fit f_1 and R. These x-bins are (1) $0<x<0.1$; (2) $0.1<x<0.4$, and (3) $x>0.4$. Data at fixed x would be further cut into bins centered at fixed hadron energy, E_h. In the dichromatic beam, data can be further subdivided according to mean neutrino energy by utilizing radial cuts in the target. These data provide a y-distribution at fixed E_h. An example of such a data set is shown in Table IV, with $37.5<E_h<62.5$ GeV and $0.1<x<0.4$. Our acceptance is folded into these numbers also.

The statistical accuracy on a nominal $\tau= 0.78$ is shown in the last column. It should be noted that this data is at only a single x,q^2 point. In the next section, we address the statistical accuracy of f_1 and R for fits to this data and at all the other points in x and q^2.

Table IV: Example of subset of data with $0.1<x<0.4$ and $37.5<E_h<62.5$ GeV. For R=0, this data would have $\tau(y) = 0.78$ independent of y.

E_o (GeV)	ν type	Radial Cuts (m)	Mean E_ν (GeV)	y	$\varepsilon(y)$	Number of Events ν	Number of Events $\bar{\nu}$	σ_τ (statistical)
250	ν_K	0- .8	225.	.22	.98	2420	99	.036
		.8-1.5	188.	.27	.96	3230	120	.028
200		0-1.5	170.	.30	.95	1960	130	.027
165		0-1.5	145.	.35	.92	1233	108	.029
140		0-1.5	125.	.40	.89	756	73	.033
120		0-1.5	109.	.46	.84	455	43	.041
250	ν_π	0- .25	99	.50	.77	3080	288	.015
		.25- .45	82	.61	.67	3620	251	.014
		.45- .65	61	.80	.37	1475	63	.021
		.65- .85	45	.91	.15	221	6	.053
200		0- .25	81	.61	.68	1040	93	.025
		.25- .45	71	.70	.54	1300	91	.022
		.45- .65	58	.82	.35	621	31	.031
		.65- .85	45	.90	.16	145	5	.065
165		0- .25	68.	.73	.48	530	40	.033
		.25- .45	62	.79	.37	680	44	.029
		.45- .65	53.	.84	.27	377	19	.040
		.65- .85	44.	.92	.13	123	5	.070
140		0- .25	58.	.81	.35	213	13	.053
		.25- .45	54.	.84	.30	290	16	.045
		.45- .65	48.	.88	.20	192	8	.056
		.65- .85	42.	.94	.10	80	3	.087
120		0- .25	50.	.86	.26	72	4	.091
		.25- .45	48.	.88	.18	106	5	.075
		.45- .65	44	.92	.15	84	3	.085
		.65- .85	39	.98	.02	14	0	.208

A. Fits to $(\sigma+\bar{\sigma})$ to obtain R and f_1 at fixed x,q^2.

Each set of data at fixed x and E_h permits measurement of $f_1(x,q^2)$ and $R(x,q^2)$ by fitting of the data with equation (9).

$$\tau(y) = \frac{\pi}{G^2ME} \frac{1}{[1+(1-y)^2]} \frac{d(\sigma+\bar{\sigma})}{dx\ dy} = f_1(1+\varepsilon R) \qquad (9)$$

Figure 7a, b, c show the standard deviations $\sigma(f_1)/f_1$ (circles, lower curves) and σ_R(crosses) in 4 bins of q^2 at each x value. Note that for $x<0.4$, errors on R of less than 0.05 at each q^2 are to be expected. For higher x, the statistical accuracy is less, though quite good enough to see whether R is large there. The magnitude of the structure function, f_1, would also be measured with good accuracy (±3% at low x, $\lesssim$ 8% at high x).

It should be noted that these errors come from a 2 parameter fit to equation (9). There is substantial coupling between the parameters (R and f_1). <u>If we assumed that R≡0, the error on f_1 would be typically a factor of 3 to 4 smaller</u>. Most previous analyses of f_2 have assumed just this. There is, of course, no good experimental or theoretical reason to assume it.

With data in hand, it might be binned differently than that shown here. For example, if it turned out that there were evidence that R = 0 independent of x,q^2 in this energy region, smaller bins in x would still give adequate statistical accuracy on f_1 (for the purposes of moments, etc.).

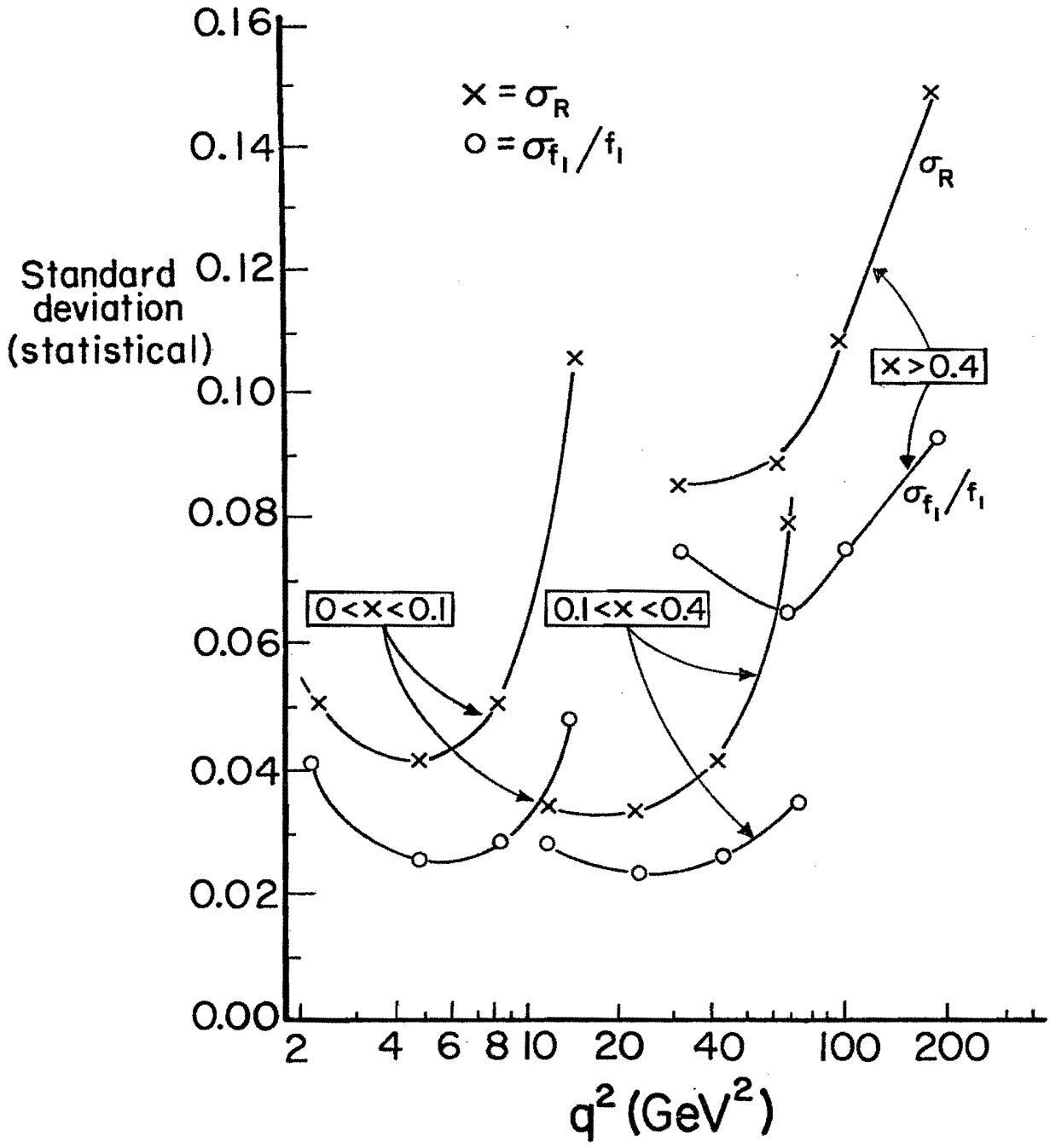

Figure 7

Figure 7: Statistical standard deviations expected for data of Table III in regions of x and q^2 for simultaneous fits to R and f_1. Note that, if R=0, the error on f_1 ($\sigma f_1/f_1$) would be 3 to 4 times smaller. The curves are drawn to guide the eye only.

B. Fits to $(\sigma-\bar{\sigma})$ to obtain f_3 and g_3 at fixed x,q^2.

By fitting the data of Table III to equation (1a)

$$\frac{d(\sigma-\bar{\sigma})}{dx\ dy} = \frac{G^2ME}{\pi}\ [f_3[1-(1-y)^2] + g_3[1+(1-y)^2]]$$

We expect to obtain the statistical errors, at various x and q^2 values, as shown in Figure 8. Tests of charge symmetry (g_3) between 2% and 10% are possible at a variety of x,q^2 over all y. Given that g_3 may be constrained by theoretical knowledge and prejudice, values of f_3 are possible with statistical accuracy $\leqslant$ 3% over this range, (cross-circles-lower curves).

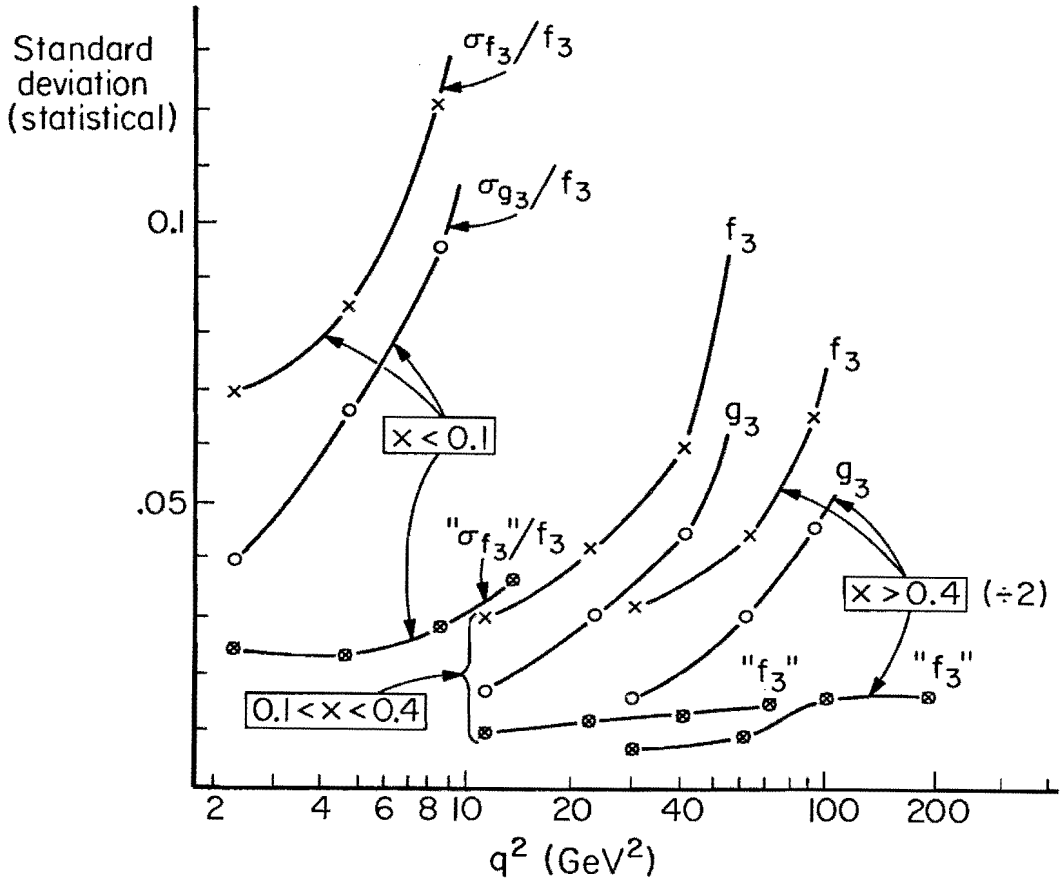

Figure 8

Figure 8: Statistical standard deviation expected for data of Table III. Upper curves give the error for simultaneous fits to equation (1a) for f_3 (crosses) and g_3 (circles). If g_3 is assumed known, the error on f_3 is given by the lower curves (⊗), i.e. "σf_3"/f_3. The values for x>0.4 should be multiplied by 2. The curves are drawn to guide the eye only.

where a systematic shift may occur (e.g. $\Delta x \sim Kx$), especially at larger x-values, where the x-distribution itself is falling. For systematic energy measurements $K \leq .015$, the shift in R should be smaller than .01 at small x ($x < 0.3$). At larger x, ΔR would be larger ($\Delta R \leq 0.05$), so that we are aiming at systematic energy measurements of 1.5% or better. This is quite feasible with calibrations made in Lab E and energy comparisons to be made in the dichromatic beam.

VI. Resolutions and Other Corrections

In an experiment of this type, the raw data must be corrected for known systematic effects. In this case, the most serious of these are due to (a) experimental resolution; (b) radiative corrections; and (c) known deviations from exact charge symmetry. The process of making these corrections is most often iterative; i.e., the "true" physical distributions are often necessary input to calculating the correction. The limiting effect of the corrections in measuring fitted parameters is two-fold: (1) dilution or "washing-out" of the statistical power of the data; and (2) the theoretical precision with which the correction can be made.

Since the present world data, even at lower energies, is not nearly precise enough to calculate these corrections with the necessary precision, we can only estimate them, using model fits to the present data. Clearly, however, if these corrections are small, we are less reliant on the theoretical calculations and the statistical accuracy is less diluted. In the succeeding chapters, we estimate the likely magnitudes of these

V. Requirements on the precision of energy and flux measurements

A. Neutrino Flux Measurements

Imprecise measurement of incident flux can create difficulties in two ways. Firstly, y-distributions are obtained by comparing cross-sections from different energy settings of the narrow band beam. Overall systematic effects are irrelevant to measurements of R, though they will effect the normalization of the f_1 and f_3 structure functions. We believe that point-to-point normalization can be obtained at order 2% with capabilities of the improved narrow band flux monitoring system (see Appendix A). The effects of energy-to-energy errors are best seen by reference to figure 3, which shows how R will be extracted. If the percentage error of point-to-point flux measurements is .02, then $R_{sys} \lesssim .02$. The second effect of flux precision lies in the need to use the sum and difference of the neutrino/antineutrino cross-sections. Calculation of the effect of a relative error, .02, between neutrino and antineutrino normalizations also indicates that $R_{sys} \lesssim .02$ in the worst case over the entire q^2, x range of this experiment.

B. Systematic Errors on Energy Measurement

For each observed event, the hadron and muon energies, as well as the muon angle, are directly measured: The effects of resolutions for these measurements will be discussed later. We concentrate here on the effects of systematic energy errors in the determination of R (i.e., $\sigma_h \equiv \Delta E_h/E_h$ and $\sigma_\mu = \Delta E_\mu/E_\mu$). The most striking effect is on the x-variable,

$$x = EE_\mu\theta^2/2ME_h \tag{10}$$

various corrections to determine how important they are to measuring the structure functions. We concentrate on the hardest problem: measurements of R. In order to illustrate the effect of each, it will be shown how the y-distributions vs. $\varepsilon(y)$ become modified. Also, we fit the distorted y-spectrum taking uniform weight in y, to determine a fake R ("R") and a fake f_1 ("f1") that one would obtain if no correction were applied.

VII. Effect of Resolution on R and f_1

The resolutions on measured variables E_μ, E_ν, θ_μ are discussed in appendices C and D. Their effect is to change the cross-section by an amount directly related to the actual x and y distribution folded against the resolution function. The equation to be fitted is

$$\frac{d(\sigma+\bar{\sigma})}{dxdy} = \frac{G^2ME}{\pi}\,[f_1\{1+(1-y)^2\}+2f_1R(1-y)] \qquad (8)$$

$$(\text{fixed } x, q^2)$$

Data is grouped into bins of y at fixed x. Hence, resolution in both x and y are relevant. Figure 9 shows the components of the x-y error matrix, assuming the direct measurement errors of this experiment, as discussed in the appendices. Figure 9 represents the situation for $x = 0.05$ and fixed $E_h = 25$ GeV. The resolution on y is identical for all x at fixed E_h, and decreases slowly at higher E_h. The resolution on x increases dramatically with x, as seen in Figure 10. This increase is due mainly to the linear increase in σ_x with x due to energy errors. Our choice of bin sizes for R-determination to a large extent matches this increase.

It should be noted that the major contribution to the x-error at small x is due to the angular resolution on the muon track. Figure 10

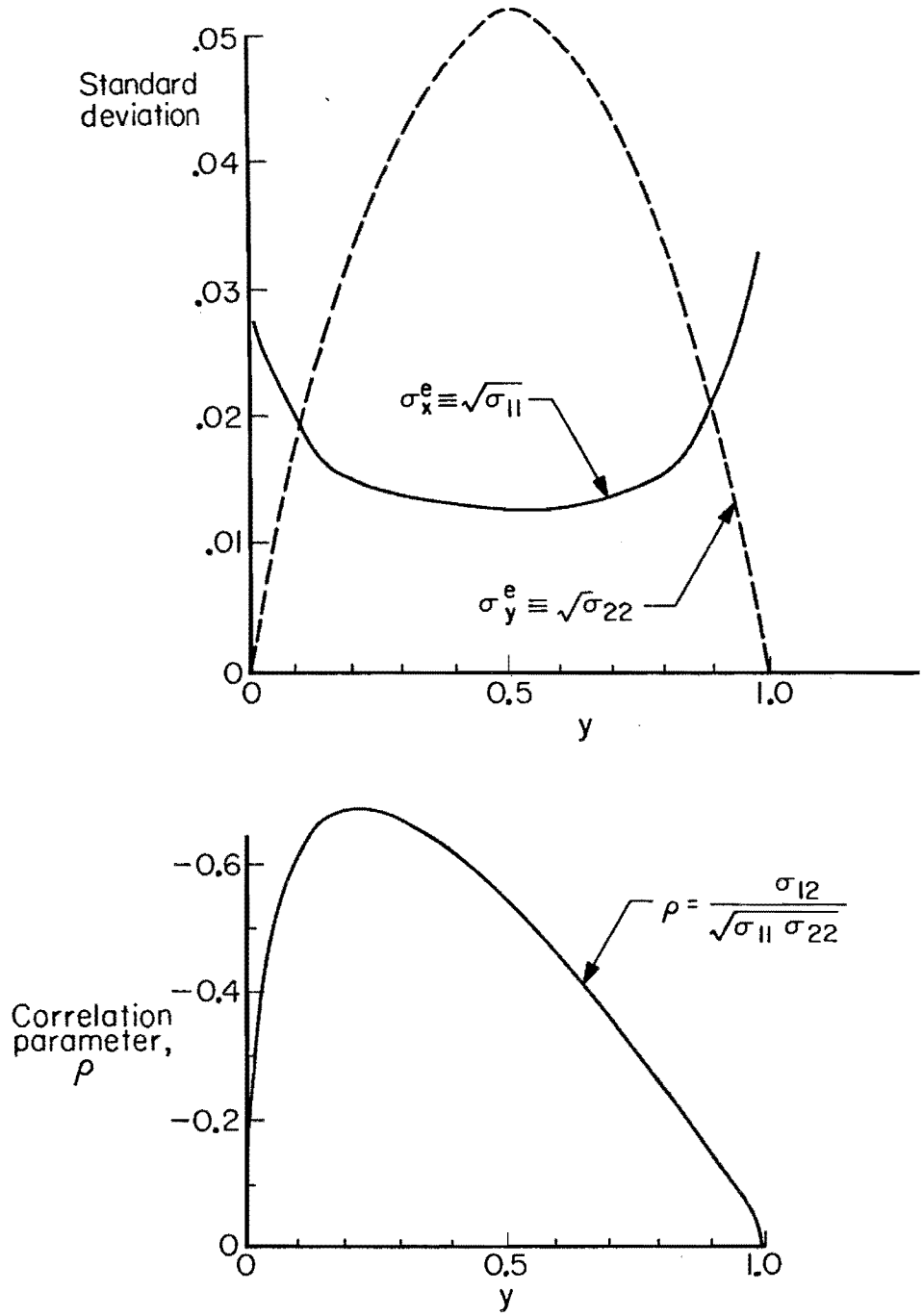

Figure 9

Figure 9 : Error matrix parameters

x = 0.05
E_h = 25 GeV

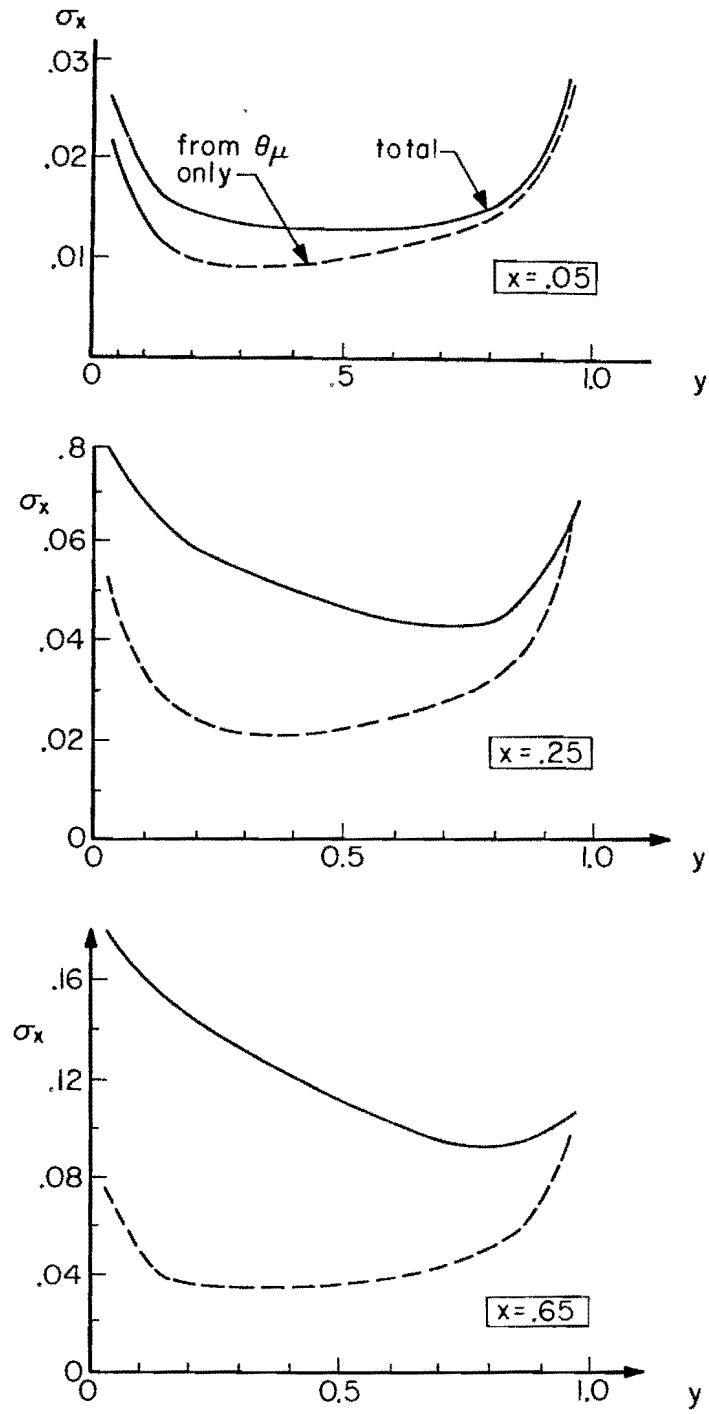

Figure 10

Figure 10: Errors on $x(\sigma_x)$ vs. y-parameter for various x-values. The hadron energy is fixed at E_h = 25 GeV. The dashed curves are the contribution from the muon angle error.

demonstrates this vividly. At larger x-values, even with our small angle errors, this contribution is still noteworthy. An experiment (see appendix E) with substantially larger errors on muon angle would have very serious corrections at small x.

The effects of these corrections is to change the observed cross-section due to "spillover" to and from x and y regions outside the bin. Figure 11 illustrates what this does in a specific case. If no corrections were applied, data that actually had $R = 0$ would have τ appear as the crosses shown in the figure. (We have assumed that the data is uniform in y). At small x and large y this correction may be as large as .08. An attempt to fit this uncorrected data would then give an apparent R ("R") and f_1 ("f_1") as shown in the linear dashed lines; a linear fit is appropriate since the data is plotted versus the propagator polarization, ε. Note that the effect on the f_1 (or f_2) structure function is comparable to the effect on R.

Table V shows what this procedure produces if we were to fit such uncorrected data at some representative points in x and q^2. Note that the worse errors are at lower q^2 and low x. But, in typical cases, the errors without corrections are comparable to expected statistical errors (see chapter IV).

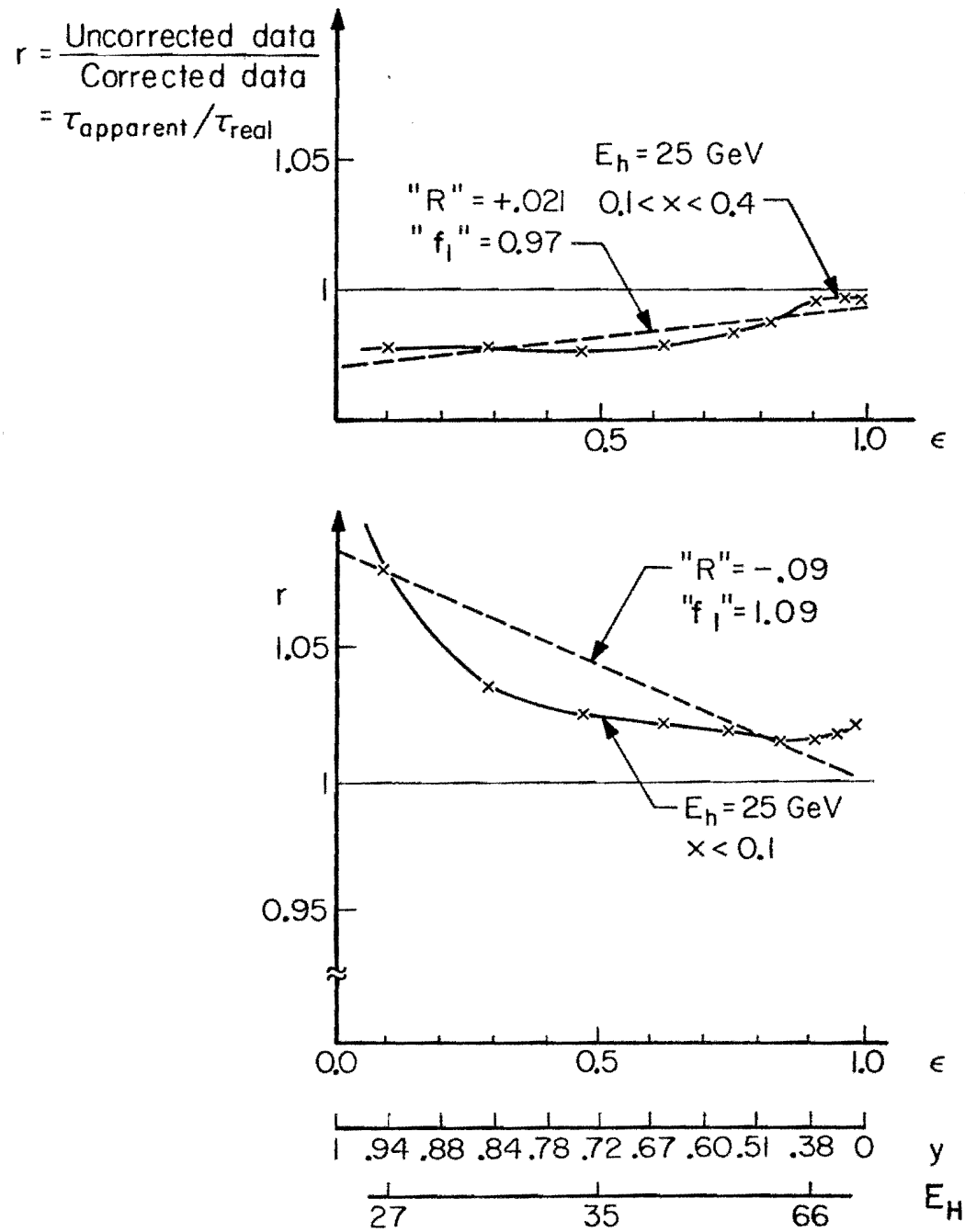

Figure 11

Figure 11: Fitted R and f, values for data uncorrected for resolutions

Table V: Apparent values of R and f_1 obtained due to resolution effects, and applying no correction.

X RANGE	E_h (GeV)	q^2 (GeV^2)	"R"	"f_1"/f_1
0-0.1	25	2.4	-.09	1.09
	50	4.7	-.05	1.05
	100	9.4	-.03	1.03
	200	18.8	-.04	1.02
0.1-0.4	25	11.7	+.02	0.97
	50	23.5	.01	.98
	100	46.9	.003	.99
	200	93.8	.002	.99
0.4-1.0	25	32.8	+.011	1.003
	50	65.7	.006	1.001
	100	131.3	.005	1.000
	200	262.6	-.005	1.002

VIII Radiative Corrections

The figure below shows some representative diagrams of electromagnetic diagrams that can modify the forms of the equations (1) and (2), and also modify the values of the structure functions themselves.

(a) Basic diagram

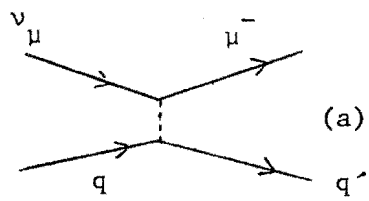

(b, c) Typical Corrections

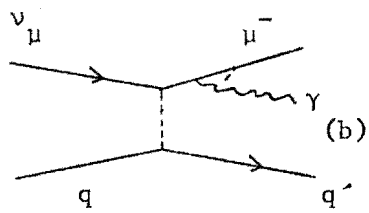

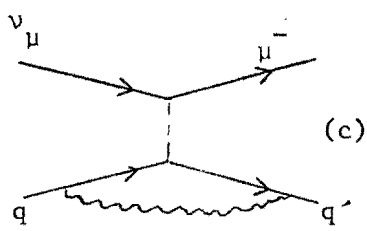

In such calculations for the inelastic scattering of muons or electrons, only corrections due to diagrams of type b are normally included. This ignores the radiative corrections to the hadron vertex, which must involve a model for their estimation. It is an allowed procedure, because the sum of all such diagrams is gauge invariant and the calculation converges.

For neutrino scattering, with exchange of charge, all diagrams at both vertices are necessary to remove infra-red divergences. Such calculations have been done,[11] using the parton model to estimate the hadronic vertex. We utilize here the major conclusions of that study to understand the magnitude of the effect expected from higher-order radiative corrections. The authors[11] found that a reasonable approximation to the correction factor, δ

$$\delta \equiv (\sigma_{\text{corrected}} - \sigma_{\text{uncorrected}})/\sigma_{\text{uncorrected}} \tag{13}$$

is, for neutrinos

$$\delta = -\ 0.0375 - 0.00020E + 0.0266\ \log(q^2) - 0.214x \tag{14}$$

and for antineutrinos

$$\bar{\delta} = -\ 0.0135 - 0.00020E + 0.0271\ \log(q^2) - 0.230x \tag{15}$$

These expressions reproduce their direct calculations to an rms error of .01 on δ.

Although in actual practice, the data would be corrected at each point, it is educational to see the magnitude of the effect produced by equations (14) and (15) on the data, and how seriously they would impact the measurement <u>if no correction were made</u>. We concentrate here on fits to equation (9), assuming R = 0 ....

$$\tau(y) \equiv \frac{\pi}{G^2ME}\ \frac{d(\sigma+\bar{\sigma})}{dx\ \ dy}\ \frac{1}{[1+(1-y)^2]} = \text{"}f_1\text{"}(1+\varepsilon(y)\text{"}R\text{"}) \tag{9}$$

There are three specific ways in which the perturbations, (14) and (15), will effect the raw data at fixed x, q^2. Firstly, there is a y-independent part that will change the value of f_1; secondly, there is an

effect due to the difference between the neutrino and anti-neutrino corrections which will introduce a term with the y-dependence $[1-(1-y)^2]$; and lastly, there is an explicit y-dependence introduced by the term proportional to neutrino energy, $E = E_h/y$. These can be individually studied by looking at the raw cross-sections as follows:

$$(\sigma+\bar{\sigma})^{raw} \approx (\sigma+\bar{\sigma})[(1-\delta_o)+\frac{\sigma-\bar{\sigma}}{\sigma+\bar{\sigma}}\Delta] \tag{16}$$

where $\delta_o = \frac{1}{2}(\delta+\bar{\delta})$, $\Delta = \frac{1}{2}(\delta-\bar{\delta})$ are the average and difference corrections, respectively. From (14) and (15), then

$$\delta_o = -.0255 - .00020E + 0.0269 \log(q^2) - 0.217x \tag{17}$$

$$\Delta = -.012-0.0002 \log(q^2) + 0.008x \tag{18}$$

Although (17) does change the value of the f_1 structure function by 1% to 10%, <u>the only change from this term in the y-dependence, for x and q^2 fixed, comes from the term multiplying $E = E_h/y$.</u> We will return to address this effect in a moment.

The term (18) also changes the y-dependence, since

$$\frac{\sigma-\bar{\sigma}}{\sigma+\bar{\sigma}} \approx \frac{f_3}{f_1}\frac{[1-(1-y)^2]}{[1+(1-y)^2]} \tag{19}$$

Table VI: Characteristic values in the radiative correction difference on neutrinos and anti-neutrinos.

x	E_h	Δ	x	E_h	Δ	x	E_h	Δ
.05	25	-.026	.25	25	-.021	.65	25	-.016
	100	-.027		100	-.022		100	-.016

Since $f_3 \leq f_1$, the correction term due to (18) is always less than Δ times the y-dependence of equation (19). From Table VI, this coefficient is always less than 3% for the energy region discussed here. This same y-dependence also occurs due to non-charge symmetric terms in the structure functions (Chapter IX), where the coefficient is expected to be larger. Discussion is therefore deferred to Chapter IX.

Returning to the effect of the y-dependence of δ_o (Equation 17), the y-dependent term (at fixed E_h) goes from .005/y at E_h = 25 GeV to .04/y at E_h = 200 GeV. Although the term becomes large at small y, there is only a small range of y available at larger E_h.
A typical situation is shown in Figure 12, for E_h = 50 GeV and x = .05, where the apparent τ is plotted vs. ε. Without correction, this term might create a systematic error of order "R" $\approx$ -.015. In general, this effect should be small, and the effect itself can probably be calculated somewhat better than its magnitude.

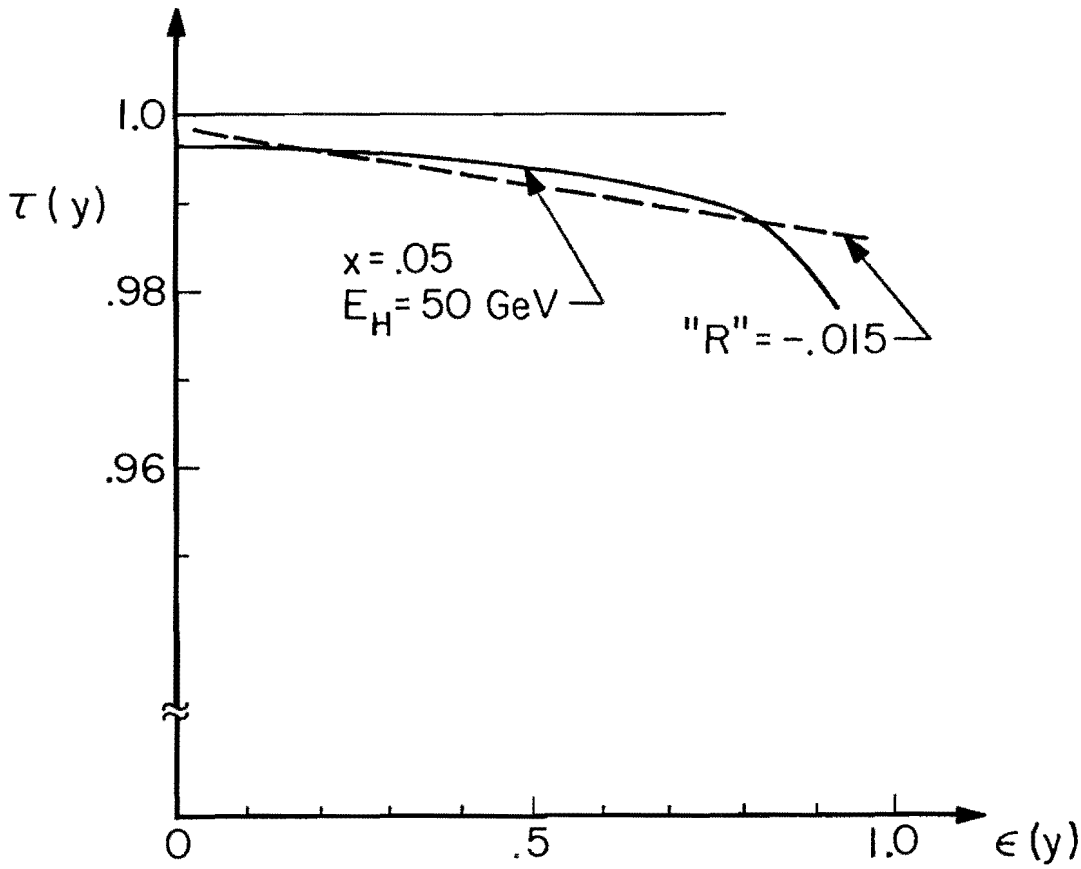

FIGURE 12

Figure 12: Calculated effect of radiative corrections on $\tau(y)$ due to term proportional to neutrino energy.

IX. Charge symmetry effects that influence y-distributions

The neutron-proton excess in an iron target, the strange-charm symmetry expected in the sea, and Cabibbo effects should create additional terms in the y-distribution that slightly modify equation (9). For R=0, these would take the form

$$\frac{d(\sigma+\bar{\sigma})}{dx\ dy} = \frac{G^2ME}{\pi}\ [f_1\{1+(1-y)^2\} + g_1\{1-(1-y)^2\}]$$

at fixed x, q^2. Here $g_1 \ll f_1$. In the quark model, these have the form

$$f_1 = x\frac{u + \bar{u} + d + \bar{d} + s + \bar{s} + c + \bar{c}}{2}$$

$$g_1 = x\frac{\delta(u + \bar{u} - d - \bar{d}) + s + \bar{s} - c - \bar{c}}{2} = \begin{pmatrix}\text{n-p}\\ \text{excess}\\ \text{term}\end{pmatrix} + \begin{pmatrix}\text{s-c}\\ \text{term}\end{pmatrix}$$

well above charm threshold. We adopt this form since the energy of this experiment tends to be well above charm threshold, and these effects get smaller at lower energy (due to threshold effects), so that the above may represent an overestimate of the actual correction.

Table VII gives an estimate of the relative size of the two terms at a few representative values of q^2 and x.

TABLE VII

q^2	x	f_1	n-p term	s-c term	g_1	g_1/f_1
9	.056	0.713	.002	.066	.070	.098
45	.206	0.505	.009	.012	.021	.041
100	.606	0.072	.004	.000	.004	0.06

Note that the effect of neutron/proton excess in an iron target is quite small over the entire x-range. The most worrisome regime is at small x, where the strange sea is largest, and is not balanced by the charm sea. The numbers for the strange component shown in the table are based on data from multimuon production. They are known to roughly 30% of their value.

There will be some uncertainty on R, at small x, due to uncertainties in this unbalanced strange sea. Figure 13 shows the form that $\tau(y)$ vs $\varepsilon(y)$ would have if <u>no correction</u> were applied with $g_1/f_1 = .095$. The effect on a fitted R is only about 1/2 this, since the y-dependence of such an effect is considerably different from $\varepsilon(y)$. (The effect on the apparent f_1 is somewhat more substantive; a systematic change $\Delta f_1/f_1 = 0.10$ may occur due to this effect.) We believe that the charge-symmetry effects on R will be corrected to give errors smaller than the statistical error.

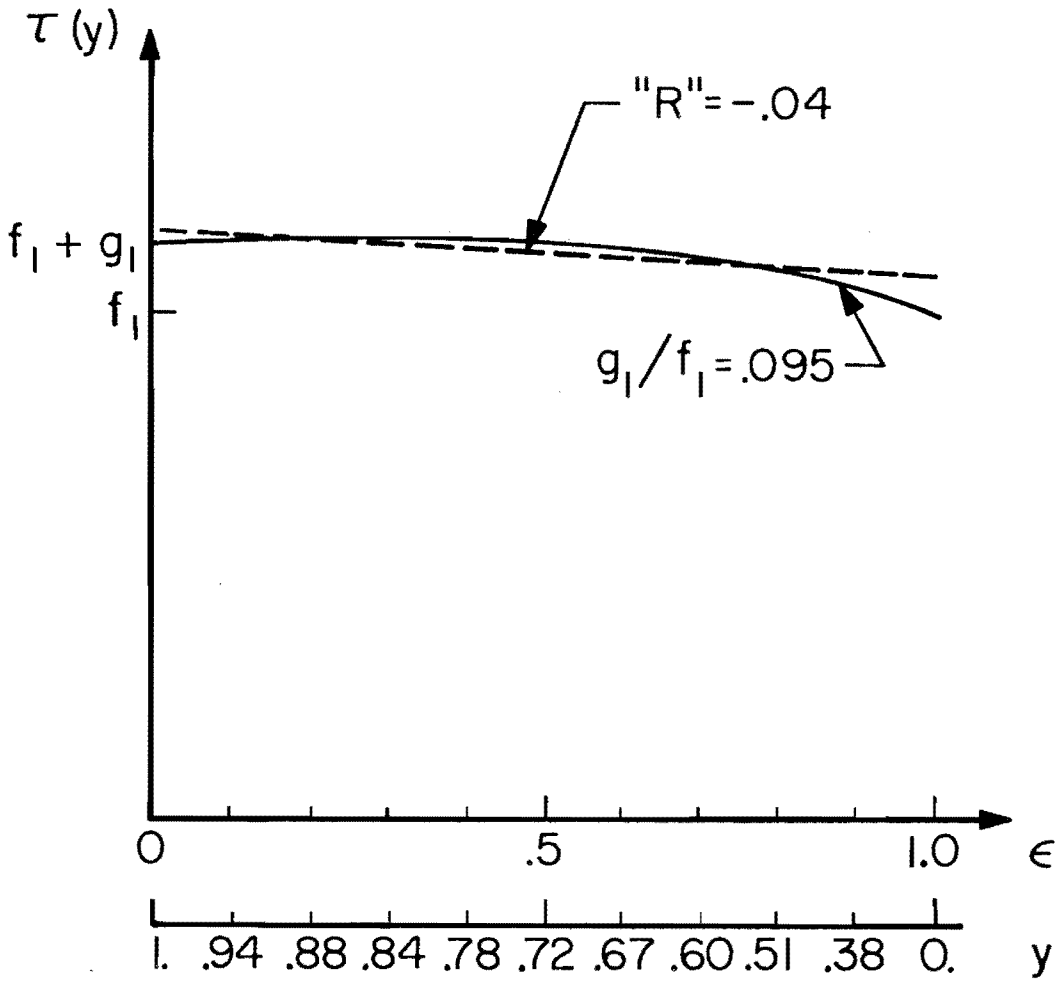

Figure 13

Figure 13: Calculated effect of charge symmetry deviations with $g_1/f_1 = .094$. The same form for the modification would result from one type of radiative correction (Chapter VIII), where $(g_1/f_1)^{eff} < .03$.

X. Needs and Requirements

To carry out these measurements, there exist certain needs. These can be divided into the following general categories:

(1) Accelerator

(2) Neutrino Beam Line

(3) Lab E

(1) Accelerator Requirements

(a) Energy: 400 GeV nominal. At the higher energy secondary settings, 450 GeV could provide important flux advantages; in some configurations, 350 GeV may not be a serious compromise.

(b) Spill: Multi 1-msec extraction. Slow spill with single 1 msec spike at the end is possible but involves some experimental compromises.

(c) Integrated intensity for data taking: 2×10^{19} protons at 400 GeV

(d) Set-up, calibration and background running: 600 hours of beam time

(i) beam checkout: 300 hours at start of run with approximately half at 400 GeV and half at 200 GeV extracted proton energy

(ii) flux calibration: 100 hours with 200 and/or 300 GeV protons of various intensities; taken late in the run

(iii) background studies: 200 hours taken under normal accelerator operating conditions (closed momentum slit on train); distributed throughout data-taking

(e) Total running time: 8 months

(2) Neutrino Beam Line

The existing dichromatic beam train is to be used. Several important modifications are necessary to respond to problems found during the E-356 run. These include:

(a) Improvement in cooling of ODT2, the dipole immediately downstream of the target

(b) Addition of vertical trim with horizontal motion in the space presently occupied by OCT, with material added in transverse region downstream of dumps;

(c) Addition of thick-walled beam pipe in the present free space between magnets OBT3 and OBT4;

(d) Additional shielding, including some boreated masonite, at the entrance to the decay pipe.

The modifications have been discussed with S.Mori and the work is proceeding.

The completion of the dichromatic flux monitoring and calibration system is essential, not only to this proposal, but for any dichromatic run. The present status of that system is shown in Table VIII,

TABLE VIII

Monitor Requirements

Neuhall	SEM - Integrating, Gated	Completed
	Toroid - Gated	"
	RF Cavity - Integrating	"
	2 SWICS with microprocessor scanners.....	In Progress
Train	2 SWICS with microprocessor scanners.....	In Progress
Expansion Port	Ion Chamber - Integrating, Gated.....	Completed
	4 Split Plate Ion Chamber.....	Completed
	SEM - Gated.....	Exists from E-21. To be used as a backup device.
	RF Cavity - Gated	To be constructed, design and acquisition complete.
	SWIC.....	Completed
	Toroid - Gated	Cores - Purchased Winding - Proceeding Shielding - to be Purchased Electronics - to be Completed
	Scanning Beam Profiler.....	Completed
	Cerenkov Counter	Exists but requires some optics modifications and a refractometer.
	Support Table Modifications....	Nearly Completed.
Target Manhole	Ion Chamber - Gated	All exist but pressure vessel requires repair
	4 Split Ion Chambers- Integrating	
	SWIC	
General	Digitizing Electronics for above	Designed but not yet constructed

(3) Lab E Requirements

Little modification is needed in the apparatus installed at Lab E. A crucial element is the completion of the E356 ADC system by March 1. If the multi 1-msec extraction is not available, some work will be required to modify the trigger(i.e., some additional PREP modules) to accommodate the slow spill portion. This will also require use of a triggering counter in the dog-house enclosure. The construction work on this enclosure is presently being completed.

One important necessary up-grade is in the on-line computer acquisition system. The additions needed are:

(a) additional 16K of memory;

(b) additional disc system to accommodate increased file storage requirements and increased disc transferred.

(c) data-way diagnostic module for each CAMAC crate;

(d) a cache memory for the PDP 11/50;

(e) unibus memory extender.

These solve our short-term difficulties, primarily of computing speed and memory shortage. In the longer term, we are investigating the use of microprocessors to process routine diagnostics, primarily on the ADC channels (pedestals, flashers, etc.). Laboratory support in this regard has been and we anticipate will continue to be very helpful.

References

(1) P. C. Bosetti et al., Nuclear Physics B142, 1, (1978).

(2) H. Anderson et al., Phys. Rev. Lett. 38, 1450, (1977).

H. Anderson et al., Phys. Rev. Lett. 40, 1061, (1978).

(3) O. Nachtmann, Nuclear Physics B63, 237, (1973).

O. Nachtmann, Nuclear Physics B78, 455, (1974).

(4) M. Holder, et al., Phys. Rev. Lett. 39, 433, (1977).

P. C. Bosetti, et al., Phys. Lett. 70B, 273, (1977).

B. C. Barish, et al., Phys. Rev. Lett. 39, 741, (1977).

(5) M. Mestayer, SLAC Report No. 214.

(6) B. A. Gordon, et al., Phys. Rev. Lett. 41, 615, (1978).

(7) See reference 1.

(8) P. Bloch, et al., Inclusive Interactions of High Energy Neutrinos and Antineutrinos in Iron, submitted to Zeitschrift für Physik.

(9) Private communication with G. Fox.

(10) Private communication with R. Field.

(11) R. Barlow and S. Wolfram, Oxford Ref. 24/78.

(12) A.Benvenutti, et al, submitted to PRL.

APPENDIX A: FLUX MONITORING SYSTEM

This measurement of structure functions requires knowing not only the number of events in a particular kinematic region but also the neutrino flux. For this reason it is appropriate to discuss our plan for flux monitoring and the status of our present measurements with the partially implemented system available in the E-356 run of Summer 1978.

The neutrino fluxes are easily calculated from known quantities (like the π and K lifetimes and the detector geometry) and the numbers of π's and K's which traverse the decay pipe (see Fig. A1). The total number of hadrons traversing the decay pipe is measured using integrating charge-sensitive devices (toroid, etc.) and the $\pi/K/p$ ratios is measured with an integrating Cerenkov counter.

It is well recognized that measuring fluxes to the desired 2% level is a very difficult problem. We have planned for a system of flux monitors which we feel will accomplish this. This system has a strong degree of redundancy for two reasons: (1) different types of monitors have different systematics, and (2) redundancy is necessary to demonstrate the accuracy achieved. For example ion chamber responses need to be corrected (by up to ~10%) for particle velocity dependent ionization effects. A toroid or RF cavity is not subject to this correction. The toroid has a signal-to-noise problem making it hard to measure low intensity fluxes while the RF cavity is subject to beam structure effects. The different monitors can also be absolutely calibrated using different techniques giving very important cross checks on the absolute calibration.

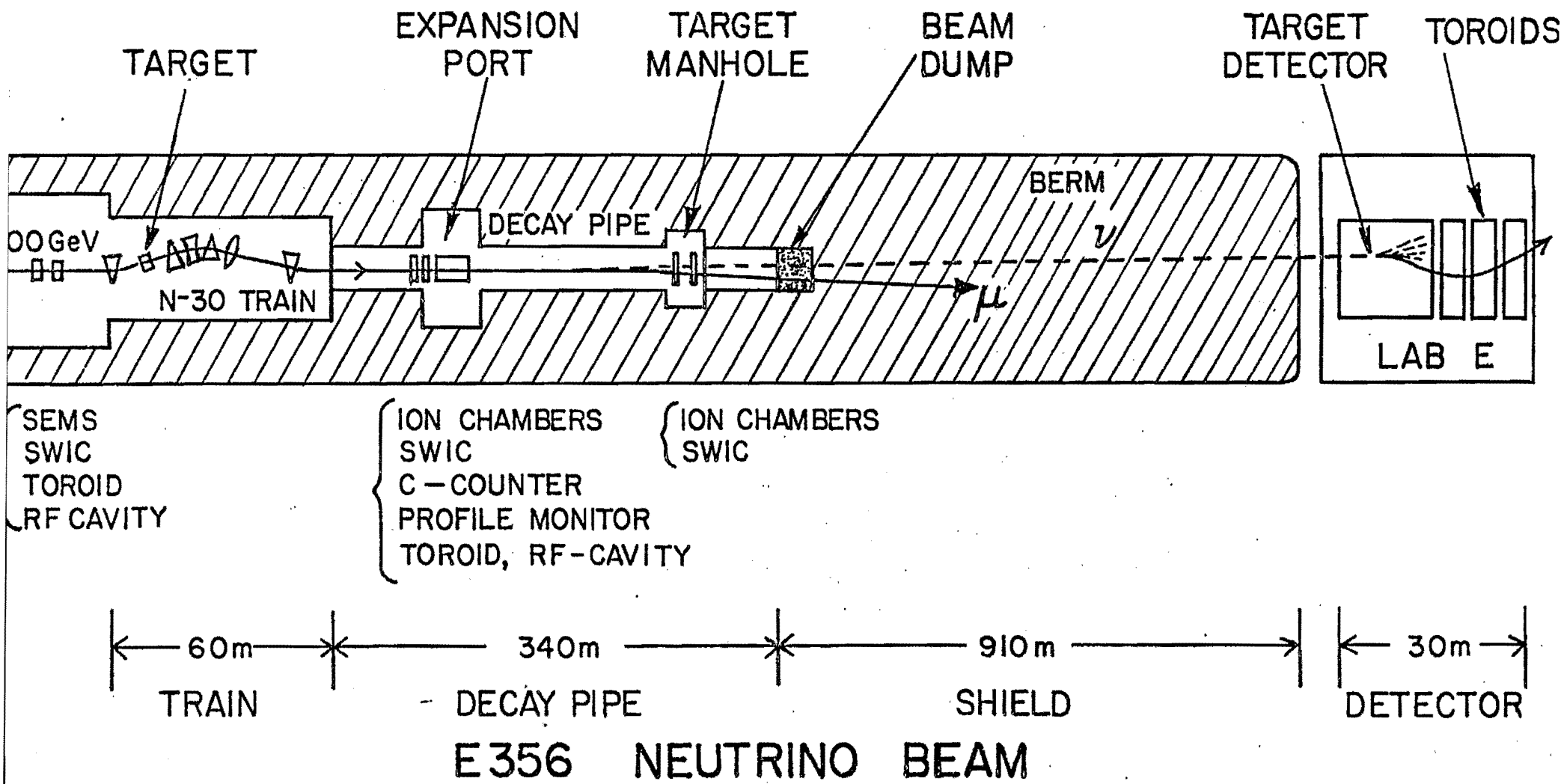

Figure A1
Neutrino Beam Line for E356

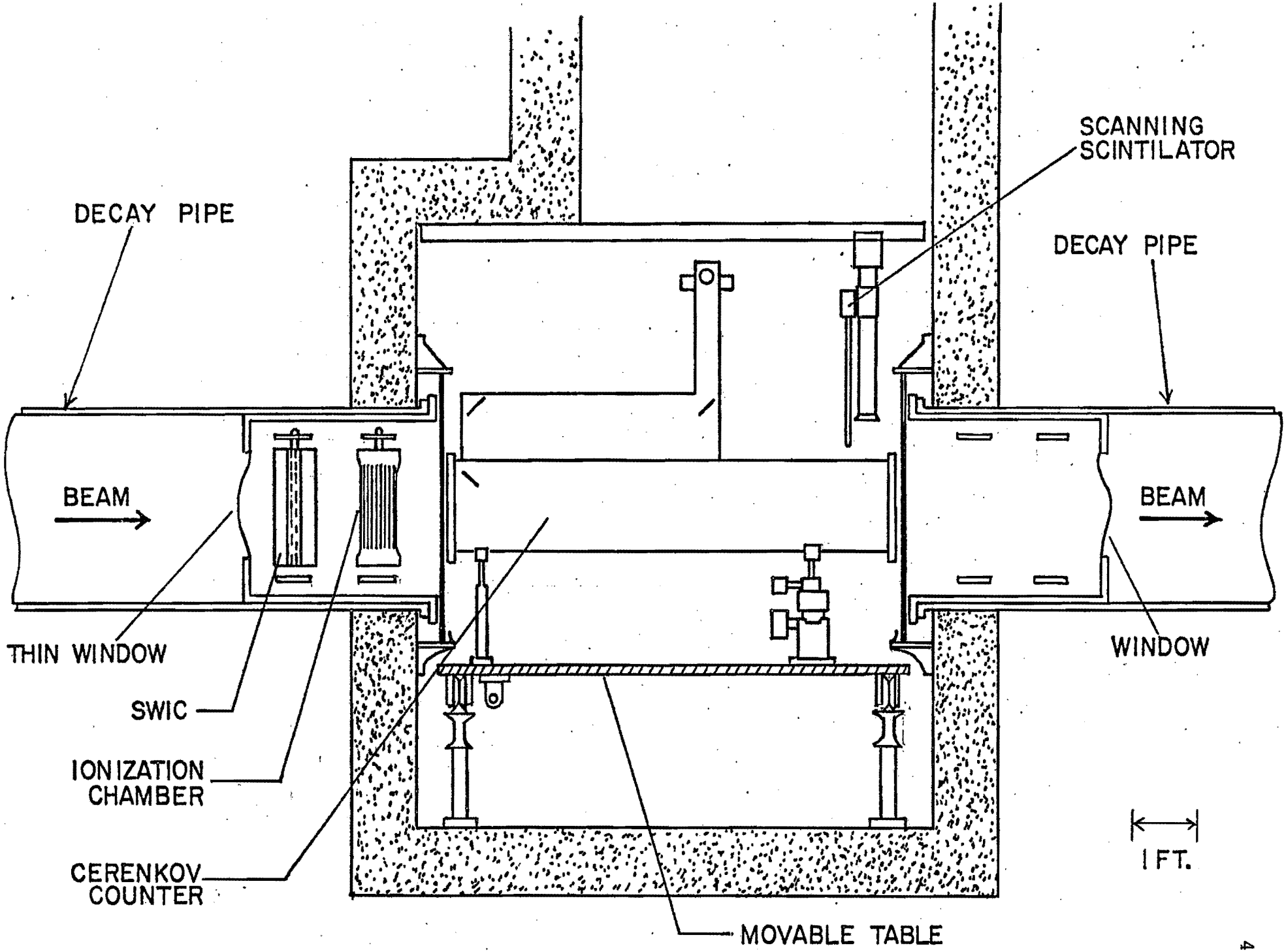

Figure A2
Expansion port instrumentation

EXPANSION PORT

The beam steering is another important factor in the analysis since neutrino energy is strongly correlated with event position at the detector. Consequently the beam steering needs to be continuously monitored and corrected when necessary. The beam neutrino energy resolution in part depends on the hadron beam angular divergence, so that it is necessary to measure this quantity.

The flux monitoring system is shown schematically in Fig. A1. The extracted proton beam flux is determined using a SEM, toroid and RF cavity located upstream of the proton target. The proton beam position and angle at the target are determined with two SWIC's.

The secondary hadron flux is measured at two locations in the decay pipe: the expansion port and the target manhole. As an example, the apparatus in the expansion port is shown in Fig. A2. A multigap ion chamber and SWIC are situated at each location. The ion chamber responds to the total flux of hadrons traversing the decay pipe. A toroid and RF cavity located at the expansion port also measure the total hadron flux. Split plate ion chambers and SWIC's at the two locations monitor the beam position and profiles.

These devices monitor, steer, and calibrate the total hadron flux while an integrating Cerenkov counter located at the expansion port determines the $\pi/K/p$ fractions.

Primarily because of budget limitations and manpower shortages, only part of this system was implemented for the initial E-356 run this summer. This partial system consisted of a toroid, a SEM, and a SWIC in the incident proton beam; an ion chamber, a SWIC, a small scanning scintillation counter and a Cerenkov counter at

the expansion port. The target manhole ion chamber was installed and debugged near the end of the summer run. We proceed to discuss the status of our studies with this partially implemented system.

1) Flux Monitoring and Steering

The hadron flux is continuously monitored with thin plate ion chambers. These chambers have been determined to be quite linear over the range of fluxes encountered in the experiment. Figure A3 shows a plot of the expansion port ion chamber response vs. the incident proton beam SEM response. From this and other evidence, it is known that the ion chamber is linear to better than 1% over the range of 5×10^9 to 1.5×10^{11} particles per pulse.

The ion chamber stability can be checked by comparing the response from the expansion port ion chamber with that of the target manhole ion chamber on a pulse-by-pulse basis. This comparison was not available for the initial E-356 run, due to the late availability of the target manhole instrumentation. However, similar ion chambers were found to be stable to better than 1% during the E-21 data run.

The old E-21 integrators, which were designed for slow spill, were used for the E-356 run. As a consequence of using 2 msec spill, these integrators were not satisfactory. This resulted in a measured 7% correction to the 300 GeV data. These integrators will be replaced with units specifically designed for the short spill encountered in the experiment.

The direction of the secondary beam is continuously monitored with two split plate ion chambers in the decay pipe. We have the sensitivity to keep the image of the beam centroid stable at the

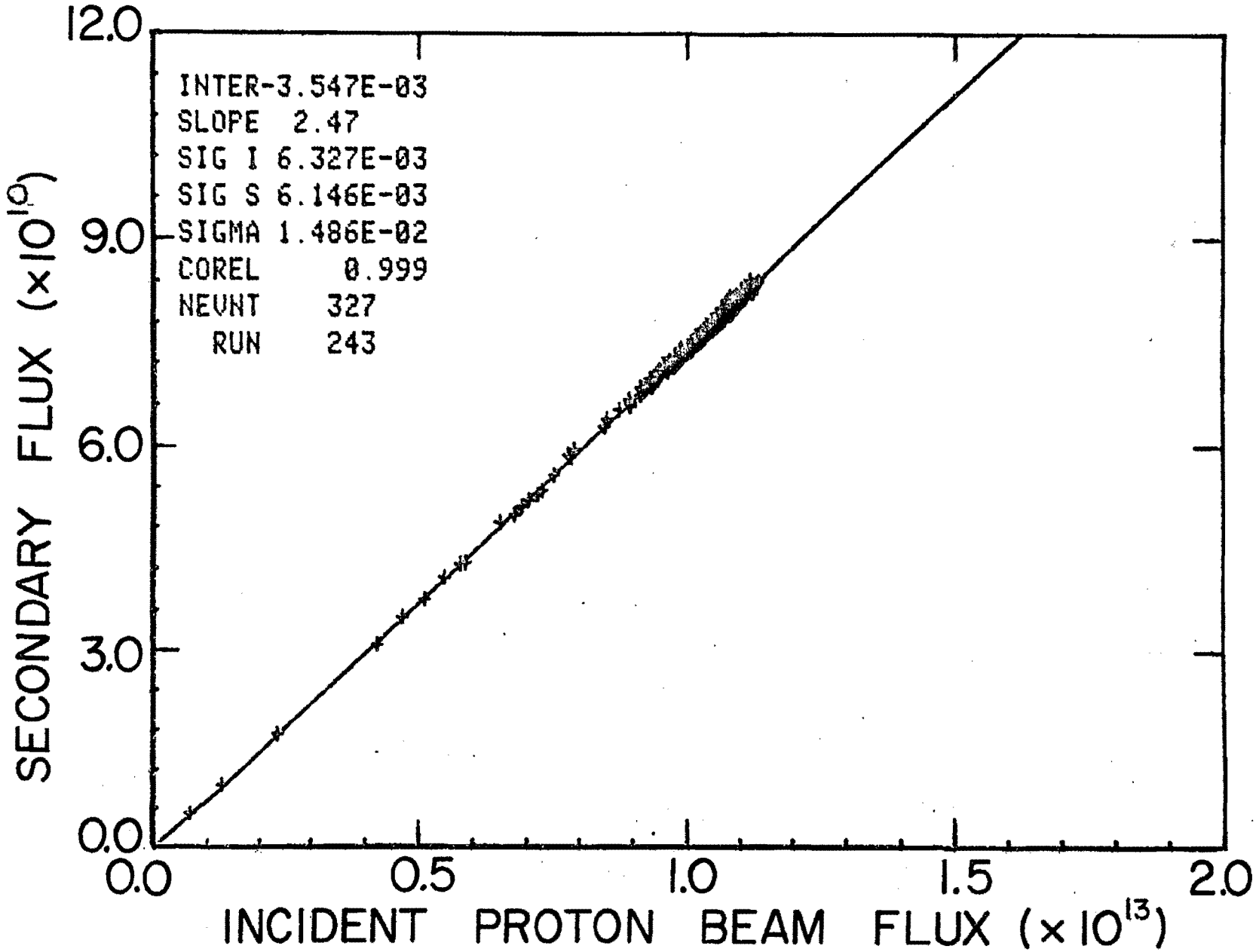

Figure A3
Linearity of Ion Chamber response

neutrino detector to better than one inch. This stability is necessary because of the strongly forward-peaked pion neutrinos. Figure A4 shows the transverse profiles for ν_π events observed in last summer's run.

2) Absolute Flux Calibration

The calibration of absolute hadron intensity will be performed with techniques involving a current transformer and RF cavity, as described previously. We expect that this can be done at the 1-2% level. In last summers run, these devices were not yet available, and so we rely on the more traditional techniques as implemented in E-21, which can be calibrated with foil irradiation and low intensity particle counting. These have known limitations at the 5% level.

The ion chamber calibration for E356 was determined by passing a 200 GeV/c proton beam through the dichromatic train into the ion chamber and a copper foil. A foil activation analysis provided the absolute calibration. As a cross-check, we compared this calibration with one done by counting particles during the E-21 run. There, an ion chamber was placed in a Meson Lab beam and calibrated by counting the particles which passed through it. This calibration agreed with the foil activation analysis also done for that experiment to 4%. The E-356 ion chambers will soon be calibrated in this way.

The monitor system as partially implemented does not provide for any improvement or verification of the absolute calibration. The addition of the toroid and RF cavity at the expansion port will

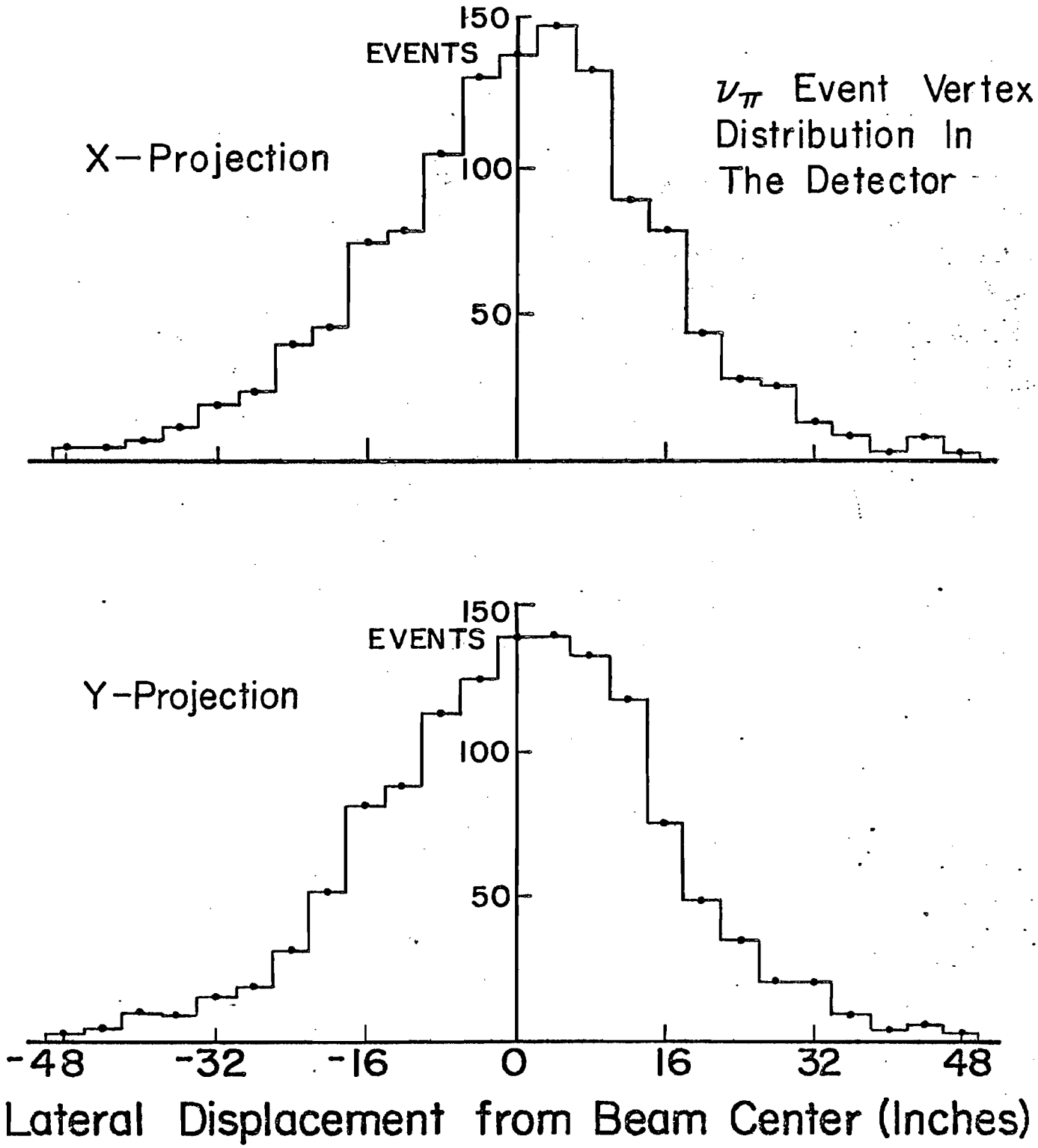

Figure A4

ν_π Event vertex distribution in the detector

substantially improve the calibration accuracy. For example the toroid can be calibrated to 1-2% by passing a known current through one of its windings.

An important uncertainty in measuring the total hadron flux was the background for high energy positive tunes resulting from secondaries produced in the proton beam dump. This background was periodically monitored by removing the target, and found to introduce an uncertainty no larger than 5%. We expect to substantially reduce the size of the background by improvements on the dichromatic train. The monitoring of any residual dumping background will reduce this uncertainty by at least an order-of-magnitude.

(3) The Cerenkov Counter

The $\pi/K/p$ particle fractions are determined with an integrating Cerenkov counter. This counter has the original vessel and optics used in E-21, with slight modifications to allow its installation in the expansion port for the initial E-356 run.

Figure A5 shows a Cerenkov curve taken at 200 GeV. The "base line" is the background created by Cerenkov light in the phototube and the glass optics. This background is directly measured by closing a shutter in the Cerenkov counter body to isolate it from the rest of the optical path outside the counter.

There exists a small residual background in a tail on the high pressure side of the peaks. We are presently taking steps to eliminate it for future running. The amplitude of the tail was measured using the incident proton beam at 200 GeV and was found to be proportional to the area of the peak. This background is also shown

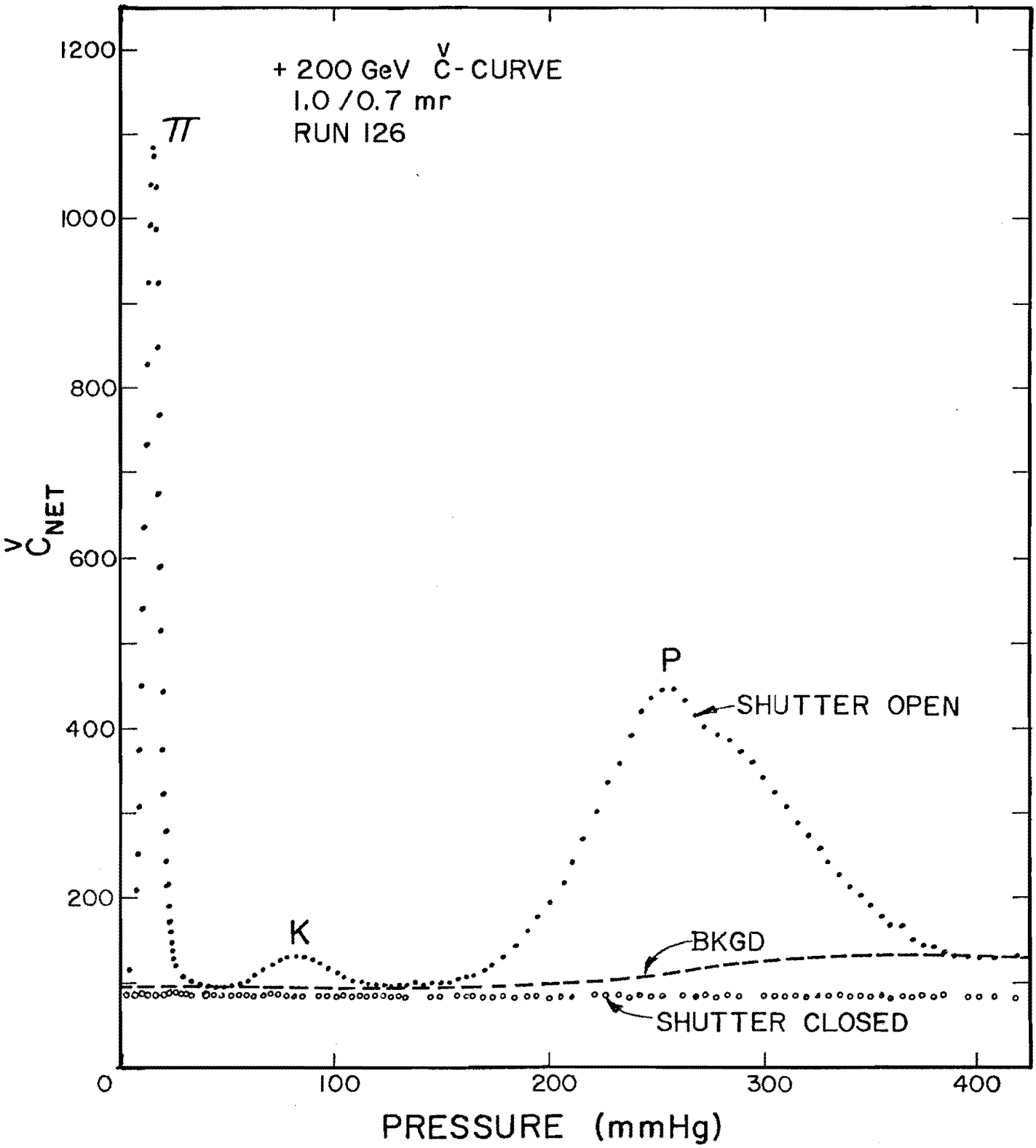

Figure A5: Cerenkov pressure curve.

in Fig. A5. For this data, the background can be reliably subtracted. The particle fractions thus obtained are shown in Figures A6 and A7 along with the older results from E-21. The E-21 Cerenkov counter used a very different technique to determine the particle fractions in that it individually counted each of the particles. The results of these two different measurement techniques are in good agreement.

The use of this counter in the integrating mode was considered to be an important test. The fact that the technique is viable means that particle fractions can be obtained in first order with accuracy comparable to a counting technique. Therefore, measurement of particle fractions can proceed without separate low intensity running conditions that replace neutrino data-taking and create difficulties for accelerator operation and extraction. With the modifications to remove the background tail and to better monitor the index of refraction, we believe that particle fractions should be obtainable at the (1-2)% level.

In summary, our minimal monitoring setup has permitted us to measure flux at an accuracy comparable to that achieved in E-21 i.e., 5 to 10%. With the completion of this system, adding the components planned originally and rectifying problems recognized in the E-356 summer run, we expect to achieve flux normalization at approximately the (2-3)% level.

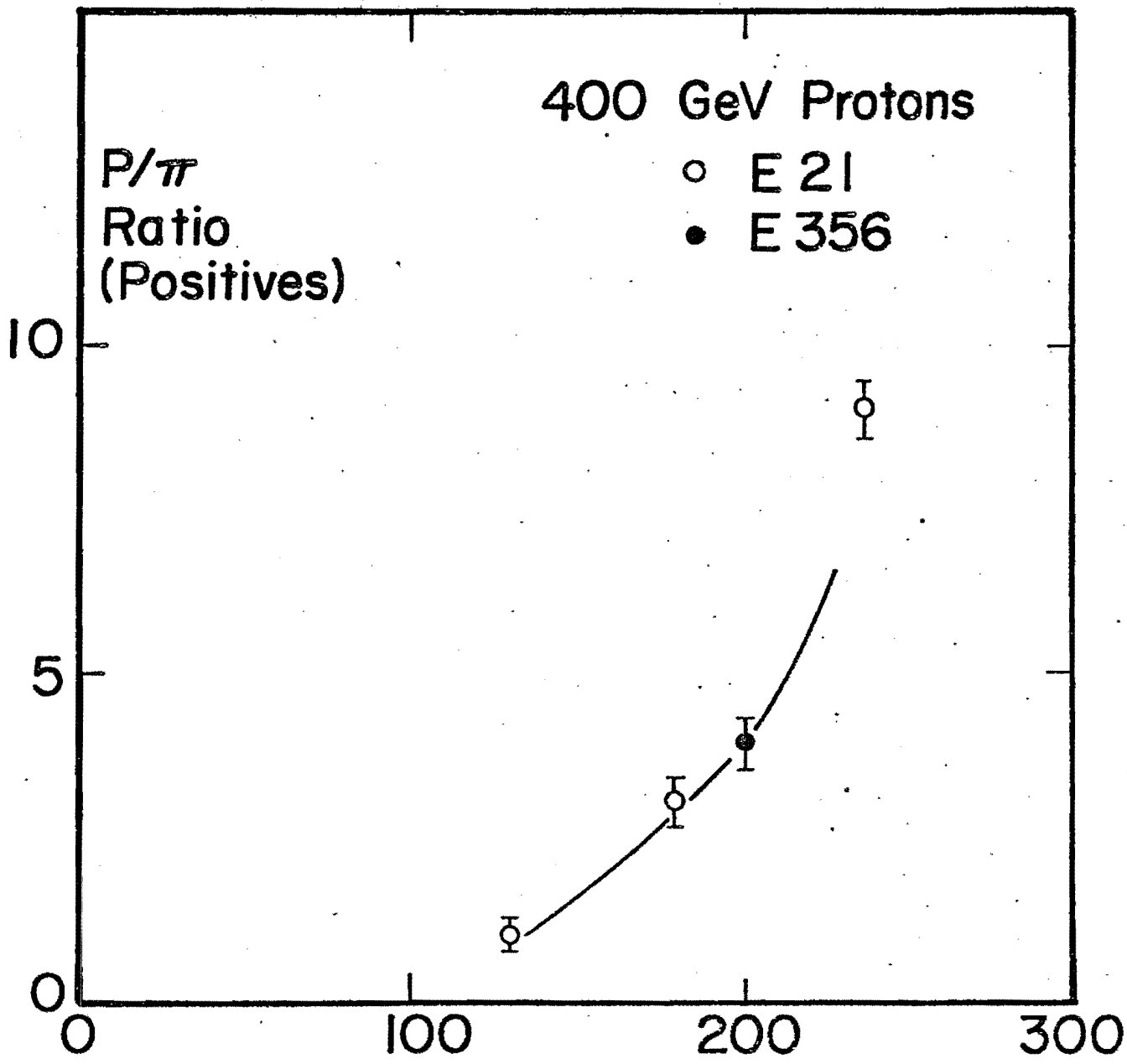

Figure A7
Positive P/π ratio

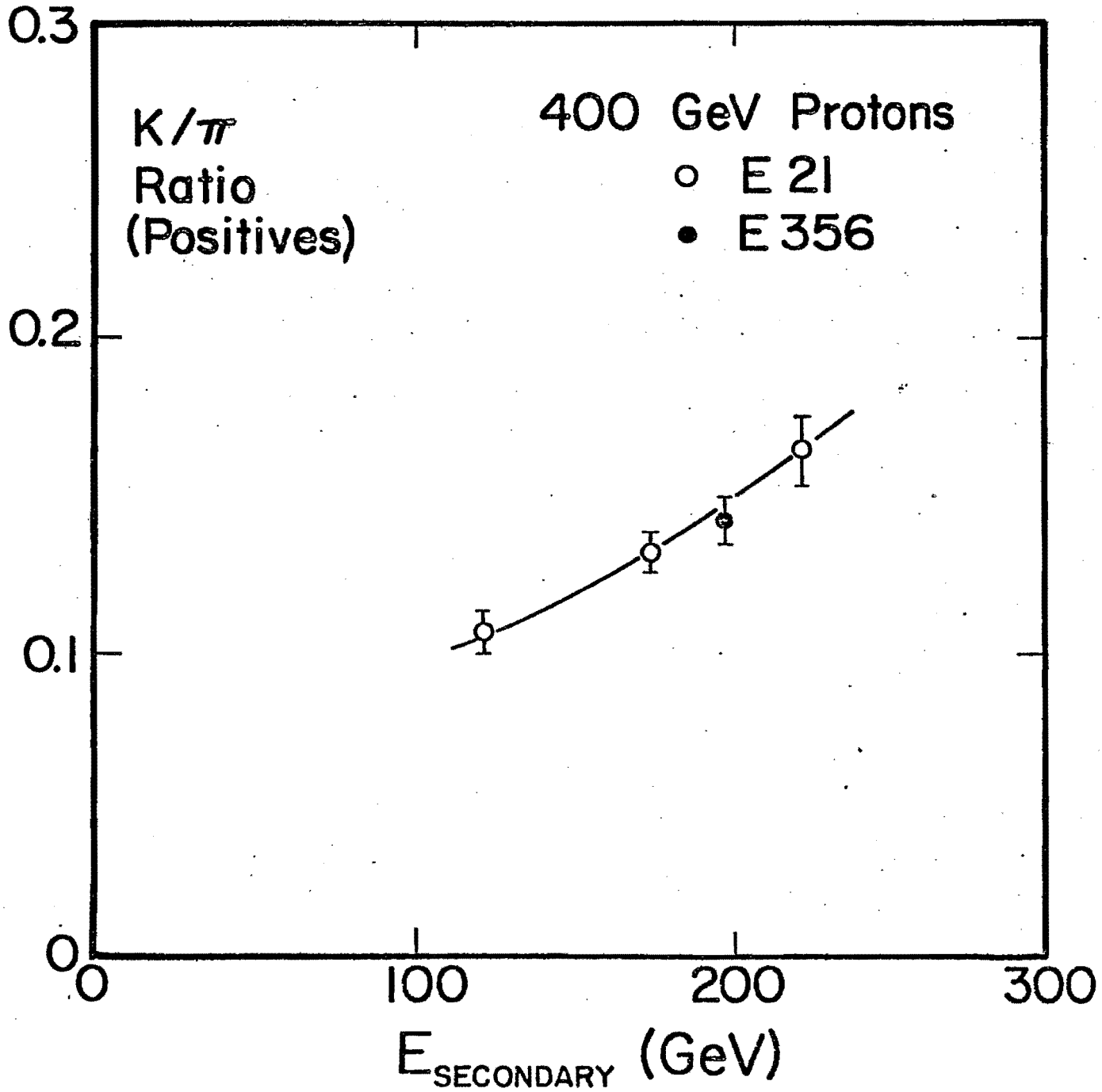

Figure A6
Positive K/π ratio

APPENDIX B: LAB E APPARATUS

The general layout of the apparatus located in Lab E is shown in Fig. B1. It consists of a 688 ton steel target with scintillation counters and position detectors interspersed to measure hadron energy and identify the trajectories of muons followed by a 404 ton instrumented toroidal magnet spectrometer which also serves as a magnetized target for neutrino interactions.

Target

The Lab E target-calorimeter consists of six modules mounted on wheeled carts. These modules move into the N5 hadron beam for calibration. Normally they reside on the N0 line for neutrino data running. As shown in Fig. B2, each target module contains 28 steel plates 10' by 10' by 2" which serve as a target and medium for hadron shower development, 14 calorimetry counters with a 10' by 10' active area to sample hadron shower development and record the presence of individual muons, and six magnetostrictive spark chambers with a 10' by 10' active area to localize the interaction vertex and trace muon trajectories through the apparatus.

Target Counters

The 10' by 10' counter planes are plexiglas tanks containing a 1" thick layer of liquid scintillator mixed with mineral oil. Wavelength shifter bars on the four sides of each counter are viewed at the corners by RCA 6342A photomultiplier tubes. The four tubes on each plane are individually pulse height analyzed to provide hadron energy. For minimum ionizing particles the four

LABORATORY 'E' APPARATUS

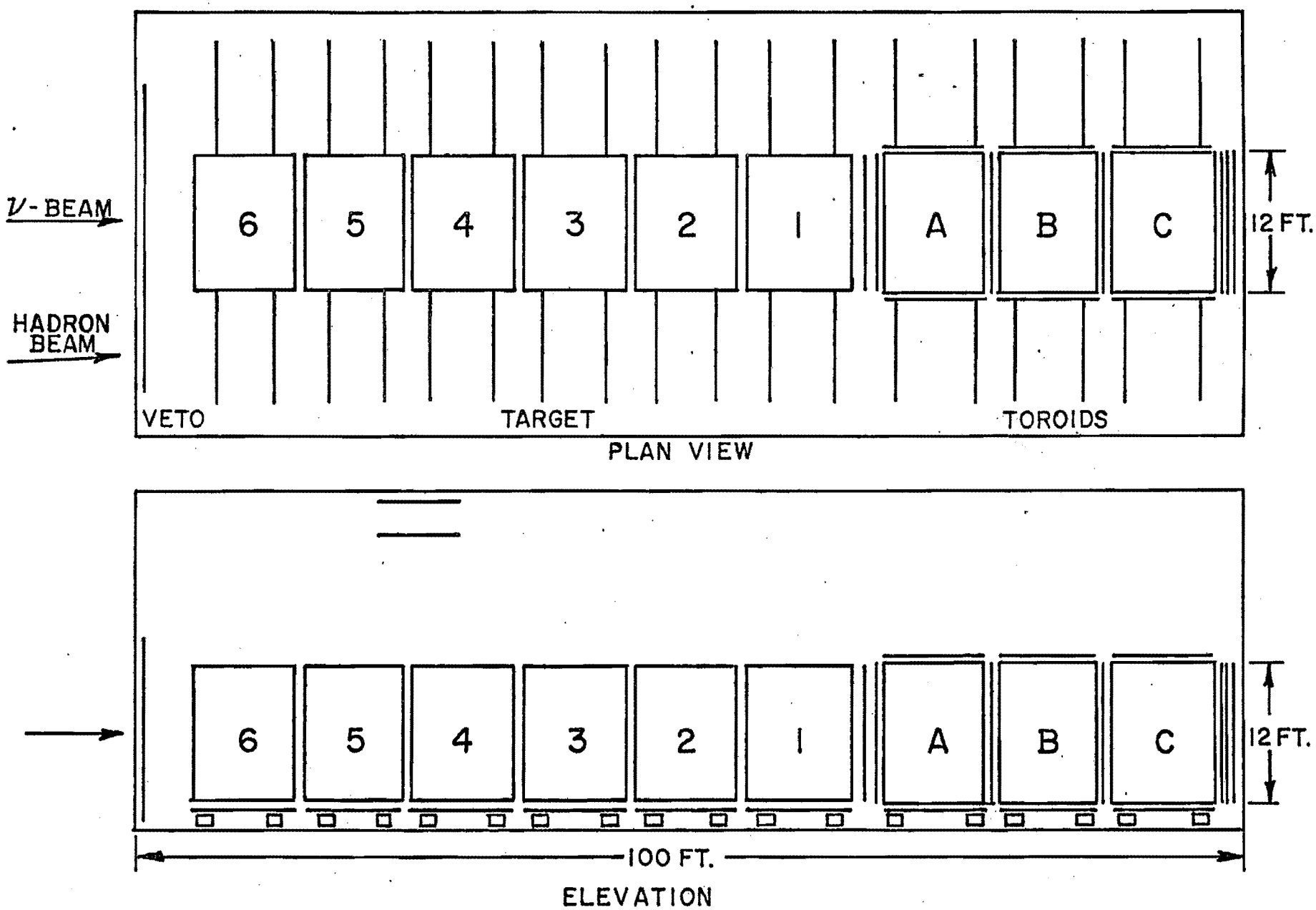

Figure B1
Lab E apparatus

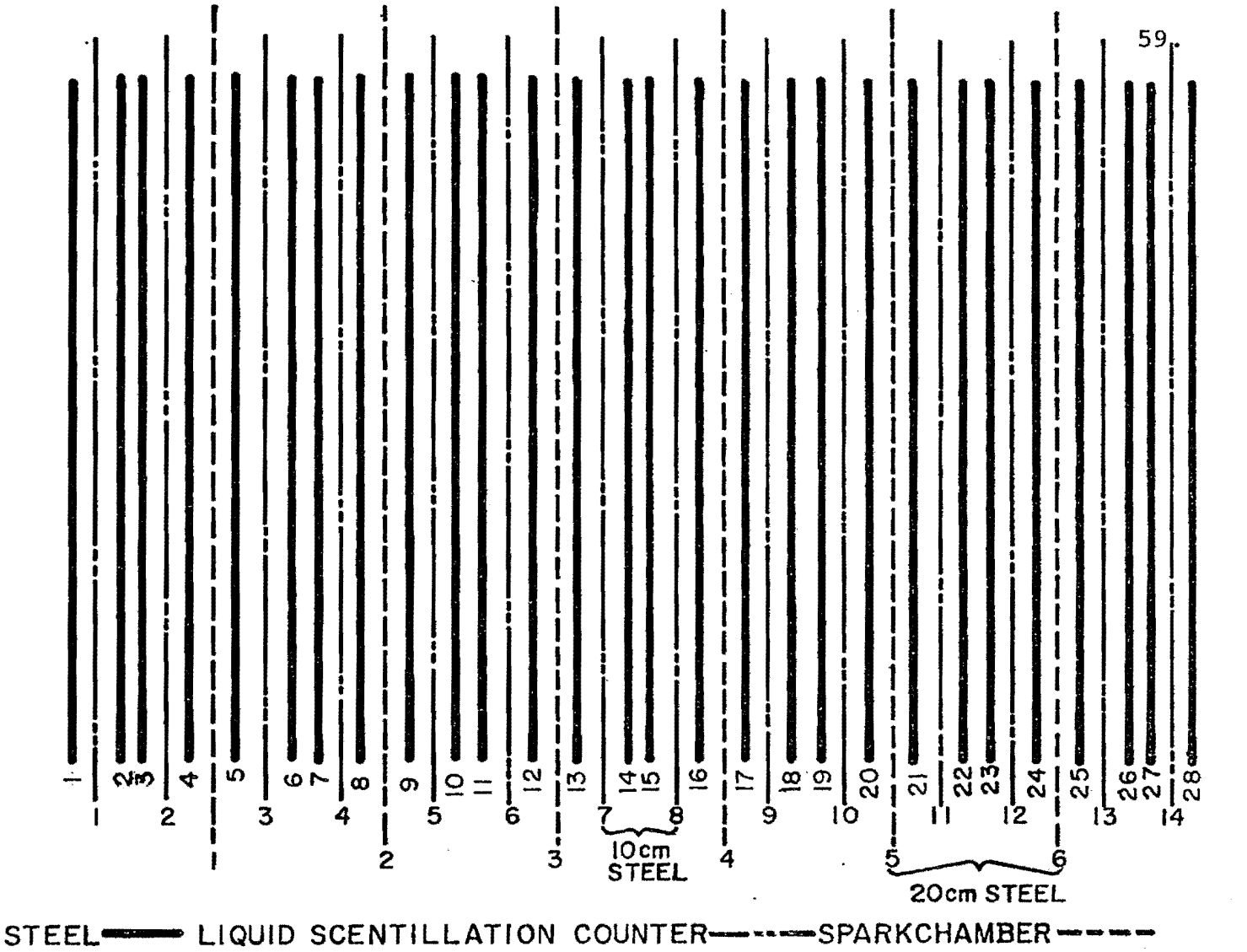

Figure B2
Target Cart Counter Arrangement

PM's are amplified by 10 and summed. Typical response to a muon through the center of the counter is 16 photoelectrons. The stability and balance for the PM's on each plane are monitored and maintained by a light flasher system. Filtered light from a spark gap is piped via a light fiber to a white dot at the center of each counter. The white dot disperses the light and allows the gain and balance to be monitored on an interspill basis. Appendix D on Calorimetry discusses linearity and resolution of the counters as a function of energy.

Target Spark Chambers

The 10' by 10' spark chambers are made from two 1" thick Hexcel aluminum clad panels with mylar-backed wires bonded to the inside. The readout is magnetostrictive. Each magnetostrictive wand contains a X3 preamplifier powered by the same coaxial cable that connects it to the readout electronics. The electronics consists of a spark chamber interface module for pulse center finding and multitime digitizers to record clock counts for the x and y mag-lines. Each chamber is pulsed by a separate low impedance, high voltage pulser which applies a 5 kV pulse of duration 200 ns. The HV pulse is derived from switching energy stored on 24 parallel HV cables via a thyratron (E.E.V.CX1164) switch to the chamber. This insures good multitrack efficiency as is demonstrated in Fig. B3 which shows a trimuon event from our Summer 1978 run.

Toroid Spectrometer

The spectrometer assembly consists of three iron ion core magnets instrumented with a total of 36 5' x 10' magnetostrictive

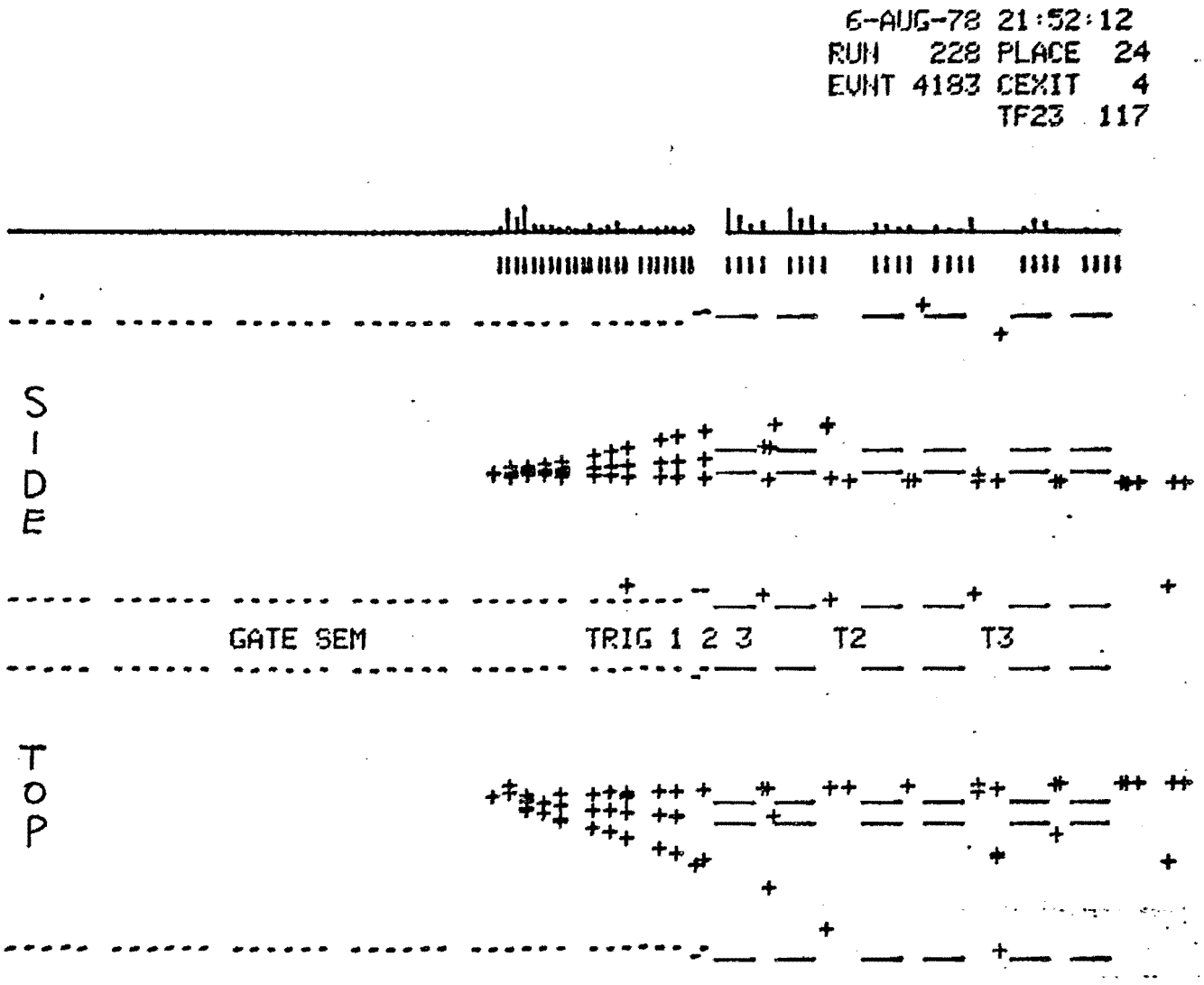

Figure B3

Tri-Muon Event

TOROIDS

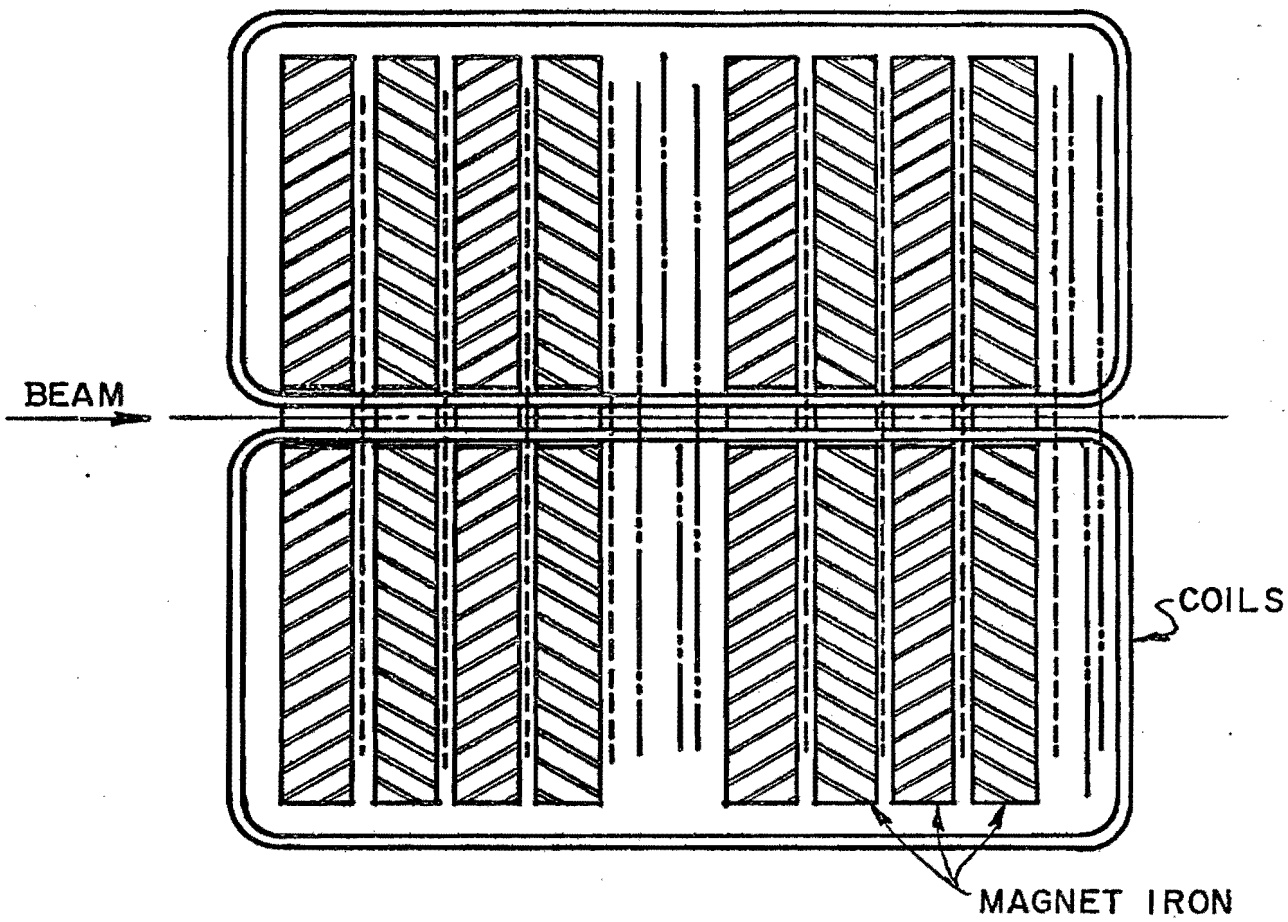

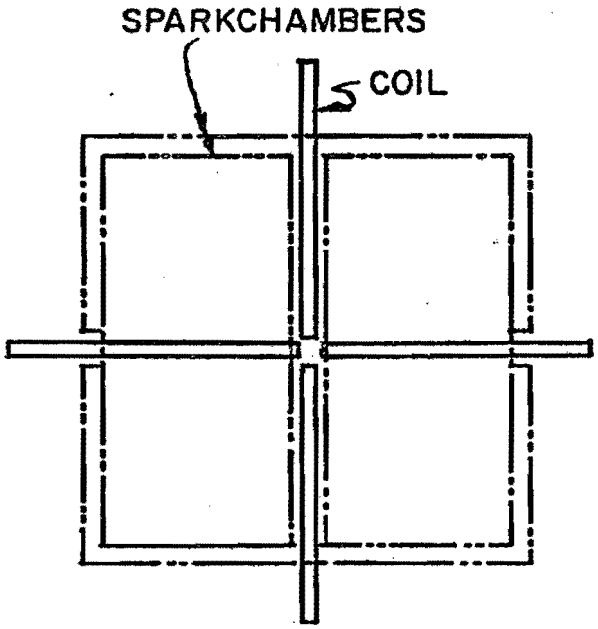

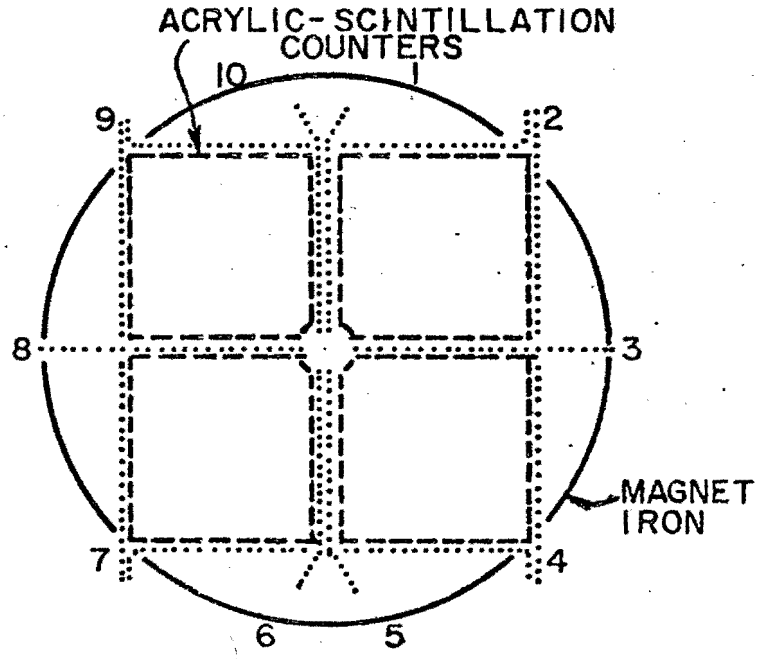

Figure B4
Toroid counter arrangement

spark chambers and 24 planes of acrylic counters doped with scintillator (Fig. B4). Each of the three spectrometer magnets can be independently translated into the hadron beam for calibration. The 11.5' diameter toroids are made of eight donut slabs of 8" thick steel. There is a 10" diameter hole in the center of the steel for the four sets of coils which power the magnets and the top and bottom halves of the steel are separated by a 3/8" air gap to facilitate field measurement. The average field of 17 Kg over the 16' length of the three toroids provides a total transverse momentum kick of 2.45 GeV/c. As discussed in Appendix C the multiple scattering in the steel gives a muon momentum resolution slightly greater than 10.5%. A very small fraction of the muons interact in the steel (i.e., deep inelastic muon scattering, high energy delta rays, etc.) leaving behind a significant amount of energy. Events of this type are easily recognized by measuring the muon with wire spark chambers which are interspersed between various sections of the 8" thick steel slabs and by pulse height in the counters which are located after every 8" of steel. The arrangement of counters, spark chambers, and steel also allows the toroids to be used as a magnetized target for neutrino interactions.

Toroid Counters

The 24 toroid counter planes each consist of two half planes (Fig. B4). A half plane contains two 5' x 5' acrylic counters and associated wavelength shifter bars (Ref. D1). Five photomultipliers collect light from the wavelength shifter bars on each half plane resulting in 10 PM's per plane. As in the case of the target,

the toroid counters have been calibrated with hadrons. The energy resolution is about a factor of two larger than for the target and is given approximately as: $\sigma E_H/E_H = 2.0/\sqrt{E_H}$. The segmented counters in the toroids allow considerable flexibility in triggering, especially relative to multimuons.

Triggers

For triggering purposes there are two arrays of counters between the toroids called T2 and T3 (Fig. B3). There is also a veto counter at the front of the building to reject triggers from muons made in neutrino interactions upstream of Lab E. There are presently five types of triggers generically labeled: (1) muon, (2) hadron energy, (3) penetration, (4) multimuon and (5) straight-throughs.

The last category is muons which enter the veto counter and pass through the trigger counters between the toroid modules. They are prescaled to limit the rate at which they are collected and are generally useful for calibration and monitoring of the equipment. The muon trigger events originate in the target and then pass through T2 and/or T3. This trigger implies a muon has reached the toroid spectrometer. The penetration trigger requires particles to pass through several consecutive counters (at least minimum ionizing) and also requires some modest energy deposition in the calorimeter. It does not require any particles in the magnet. Typically the penetration requirement is 14 counters. The hadron energy trigger requires approximately 10 GeV of energy deposition in the target but makes no demand on penetration in the target or

the magnet. This trigger provides neutral current data and frequently satisfies other trigger requirements. The multimuon trigger requires greater than 1.5 times minimum in the downstream section of the target and can also be satisfied by various quadrant combinations in the toroids.

Since there is very little logic overlap in these triggers, they are rather complimentary in the regions of scaling variables which they cover. In fact there is considerable kinematical overlap and this allows for very good trigger efficiency.

Appendix C

Position Detection

Measurement of the muon angle (θ_μ) and energy (E_μ) is accomplished using an array of spark chambers and toroidal iron magnets. The muon angle is measured by magnetostrictive readout spark chambers located inside the steel target every 20 cm of iron. These chambers are pulsed by a charge line system that gives very good multi-spark efficiency and are read out by a system allowing up to sixteen sparks per chamber. The resolution is limited by multiple scattering and by setting error in the spark chambers. One very important feature of this apparatus is the ability to track the muon close to the vertex, even in the presence of energetic hadron showers. Figure C1 shows, from a random sample of events taken with 300 GeV neutrino running, a spark can be found one chamber from the vertex half the time and in the next chamber over 3/4 of the time.

The angular resolution, then can be seen in Figure C2. An appropriate parameterization is given by:

$$\sigma_\theta^{proj} \text{ (mrad)} \approx 0.3 + 68 \text{ (GeV)}/E_\mu \qquad \text{(C1)}$$

It should be noted that, in an apparatus in which the spacing of position detectors were 2-1/2 times larger, and a magnetic field were present, the standard deviation for the angular measurement would be more than twice as large as Equation (C1) over most of the energy range.

The muon energy is measured by observing magnetic deflection in traversing the toroid spectrometer. For example, the curvature fit to the track in figure C3 gives a momentum of 149 GeV. The spectrometer system consists of 24 iron discs 20 cm thick interspersed with acrylic

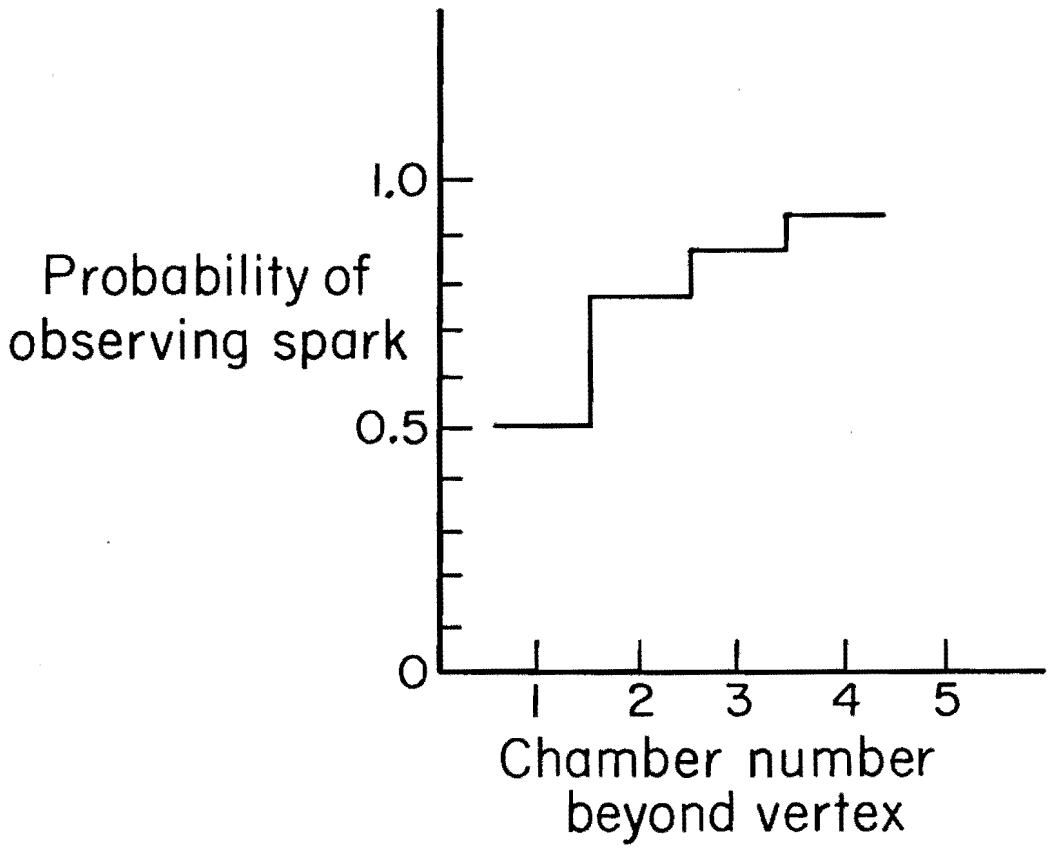

Figure C1

Experimental determination of spark presence on muon tracks near interaction vertex.

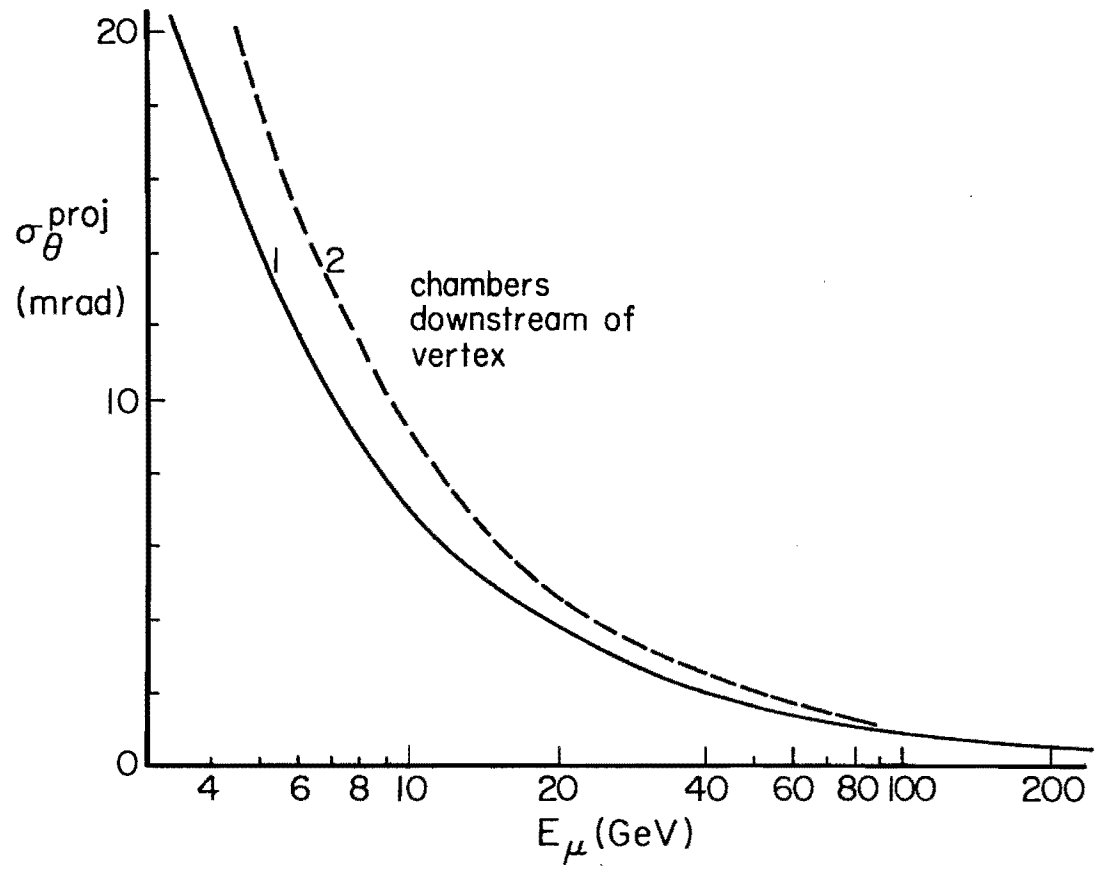

Figure C2

Projected angle error vs. muon energy for geometry of spark chambers in this experiment. Curves are shown for the first spark observed at the first (1) and second (2) chambers, respectively, from the vertex.

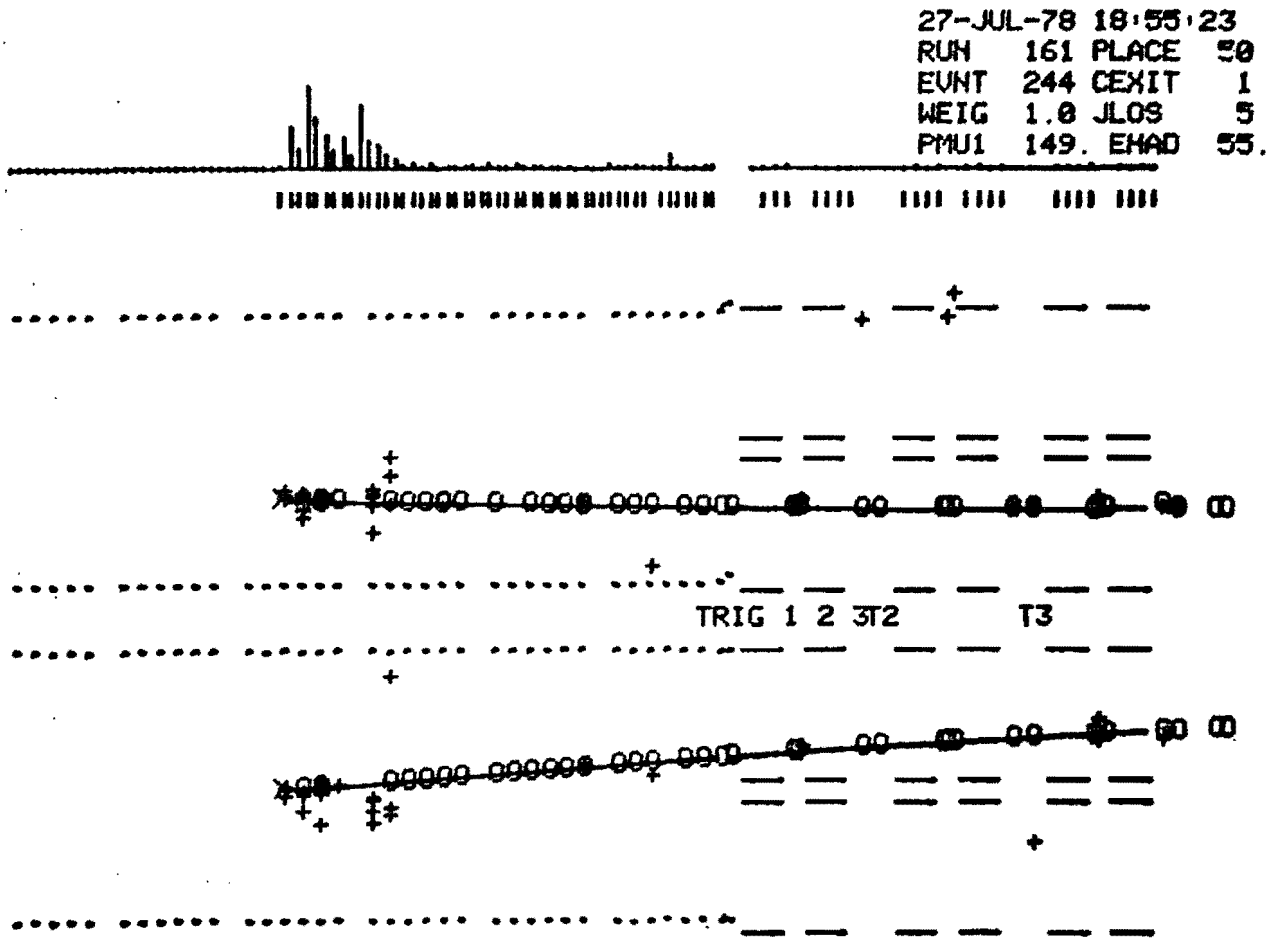

FIGURE C3

Figure C3; Typical event.

scintillation counters every 20 cm and magnetostrictive readout spark chambers every 80 cm. Events with large muon energy loss due to deep inelastic scattering or delta-ray production are sensed by detecting large pulse heights in the scintillation counters. For muon energies below 200 GeV, the momentum resolution is dominated by multiple scattering of the muon in the toroid steel. The total $\int Bdz$ of the magnets is 80 Kg-m, corresponding to a radial momentum kick of 2.4 GeV/c and a momentum resolution of 10.5%. At very high momentum, the resolution becomes limited by the setting error in the spark chambers and the measurement lever arm.

Figure C4 shows the fractional standard deviation in momentum versus momentum. Over most of the muon energy range for this experiment, the error is mainly due to multiple scattering ($\Delta p/p \approx .11$).

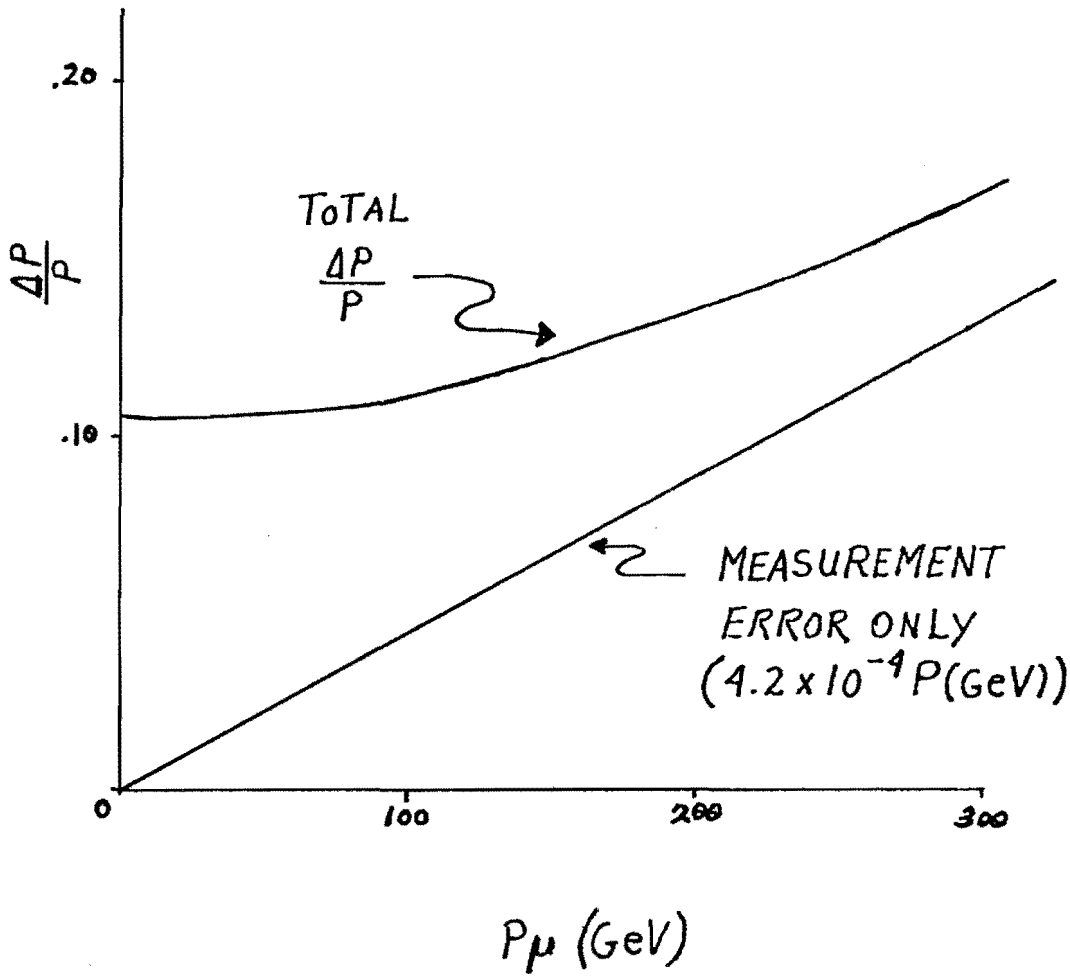

FIGURE C4

Figure C4: Fractional error for momentum measurement versus momentum.

APPENDIX D: CALORIMETRY

This section concentrates on the performance of the liquid scintillation counters in the target carts. A detailed description of these counters can be found elsewhere (Ref. D1).

Measurement of the hadron energy in a neutrino interaction is obtained from the 10' x 10' liquid scintillation counters positioned every 10 cm of steel in the target calorimeter. The light produced in these counters is collected by 8 wavelength shifter bars located on the sides of the counters. Shifter bar light is then guided into four photomultipliers at the corners of each plane. In total, there are 82 such counters in the target calorimeter arranged on six carts as described in Appendix B.

Extensive studies have been made in the N5 hadron beam line to study the response of these counters to muons and to hadron showers of known energy. Initially all counters were adjusted to give a balanced response by means of the light flasher system. Then muons were directed through the system and all counters had their absolute gain measured. For a minimum ionizing particle traversing the center of the counter, a yield of 16 photoelectrons is obtained when the pulse height of the four photomultipliers is summed. A typical pulse height distribution is shown in Fig. D1. We have investigated the linearity of response, the resolution, and the position dependence of these quantities for the entire target calorimeter as a function of energy. The pulse height distribution for 100 GeV hadrons is shown in Fig. D2. To obtain this distribution, the outputs of 56 phototubes were summed.

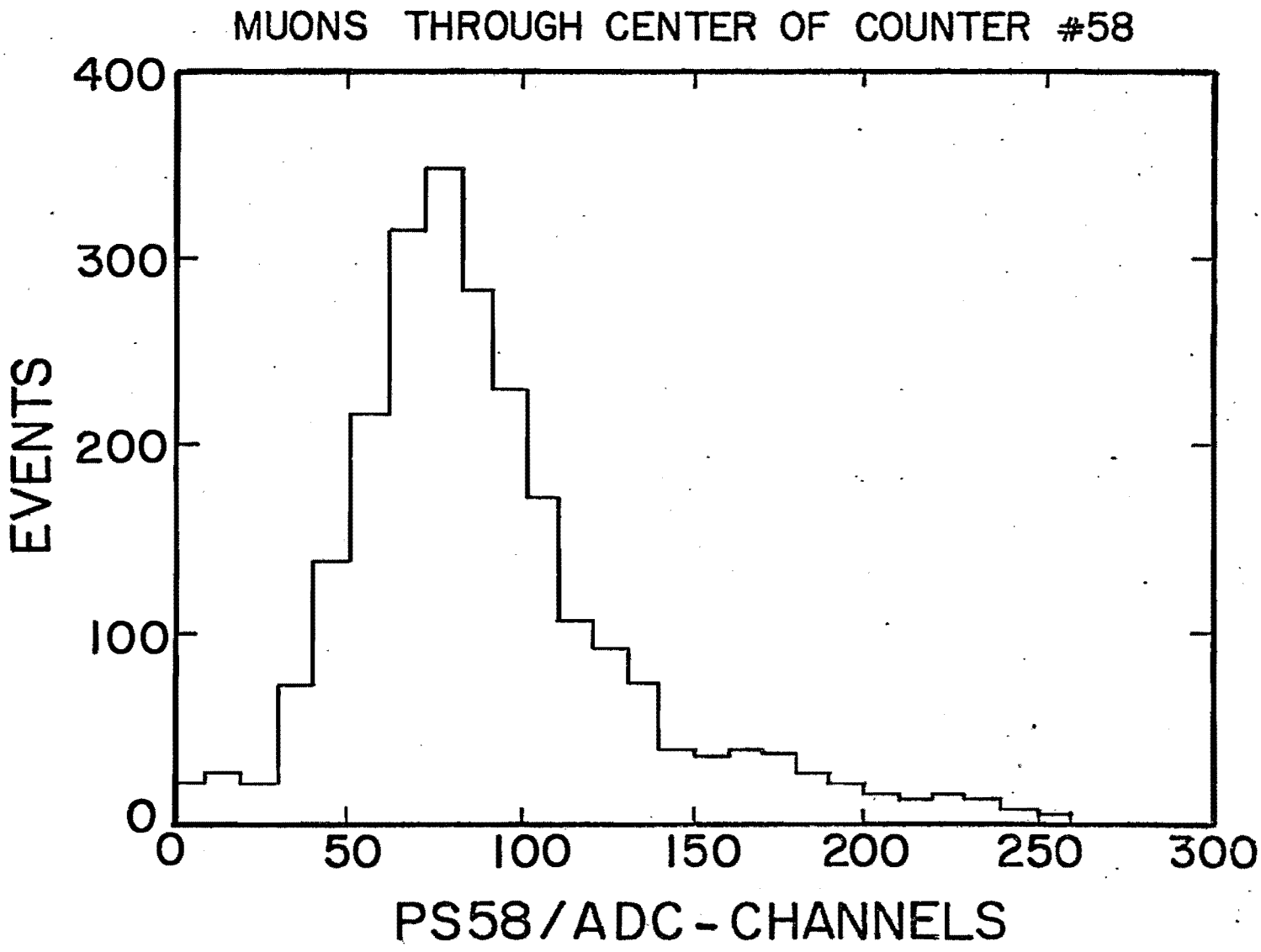

Figure D1

Pulse height distribution for muons traversing the center of a counter.

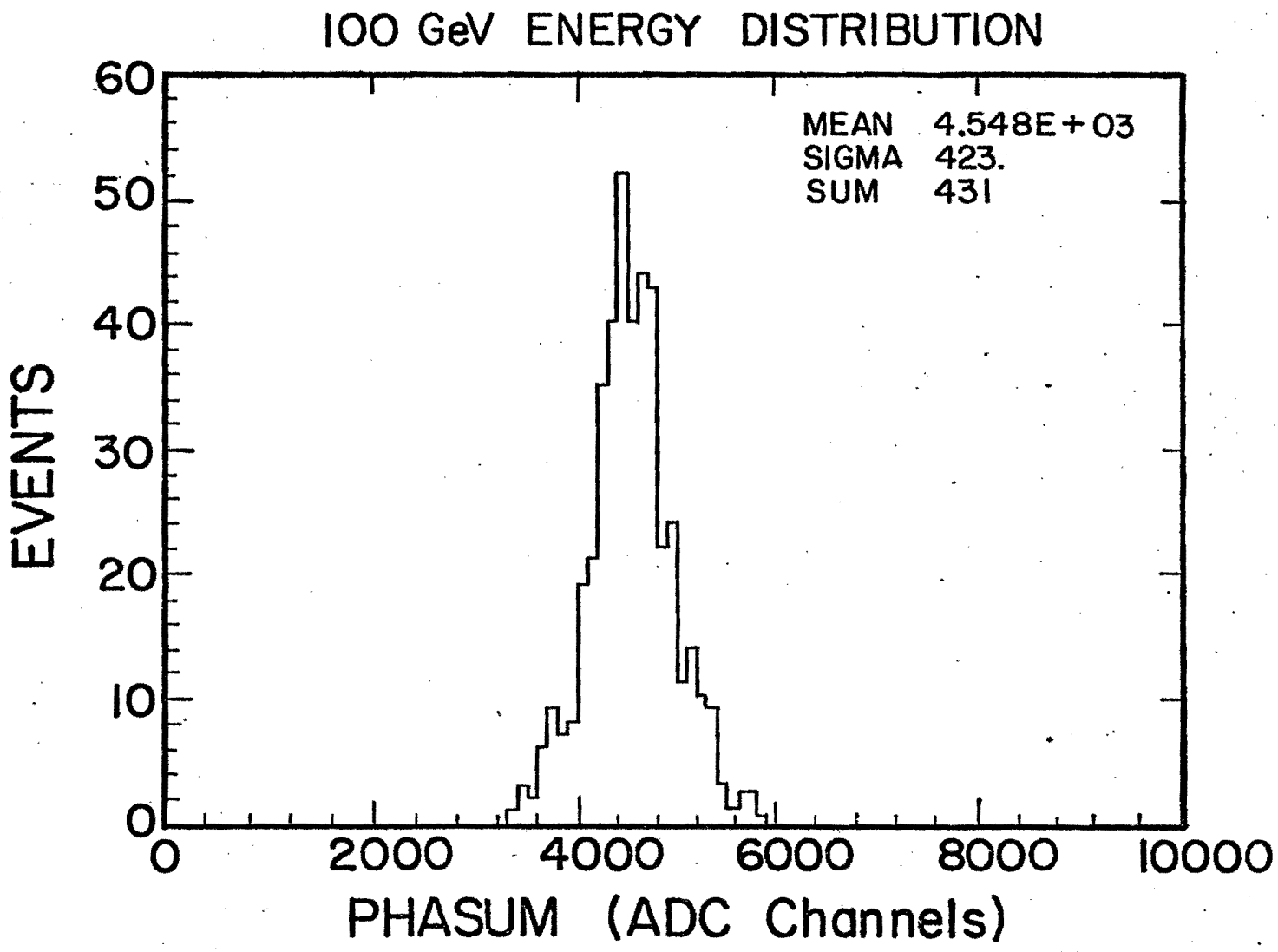

Figure D2

Pulse height distribution for 100 GeV hadrons in the center of a cart. The pulse height is summed up over 14 planes (1 cart).

The pulse height linearity between 25 and 300 GeV is shown in Fig. D3. A best fit for the response is:

Pulse Height (min. ionizing) = 4.7 x Energy (GeV).

To obtain this measurement the pulse heights of 14 counters, sampling 1.4 m of steel, were summed to avoid leakage problems. The pulse height for each plane was divided by the pulse height a muon would have at the location of the shower. The result is given in number of equivalent minimum ionizing particles. The horizontal errors shown correspond to an uncertainty of 2% in the beam energy.

The energy resolution over the region of 25 GeV to 300 GeV is shown in Fig. D4. The best fit is:

$$\sigma\,(\mathrm{GeV}) = 0.93 * \sqrt{E_H} \text{ where } E_H \text{ is given in GeV.}$$

It should be noted this resolution function is the result of on-line analysis taken with different target carts in two calibration runs separated in time by six months. It was reproducible to about 2%. In a more detailed off-line analysis, we may be able to improve the resolution further.

The dependence of pulse height on the position of the shower is shown in Figures D5a and D5b. In Fig. D5a the variation for a single photomultiplier is shown. In Fig. D5b the variation for the sum of the four photomultipliers in a given plane is listed. The sum varies by roughly a factor of 2 between a shower created in the center of the counter and one near the corner. This variation in response can be corrected by using the counter maps derived from muons.

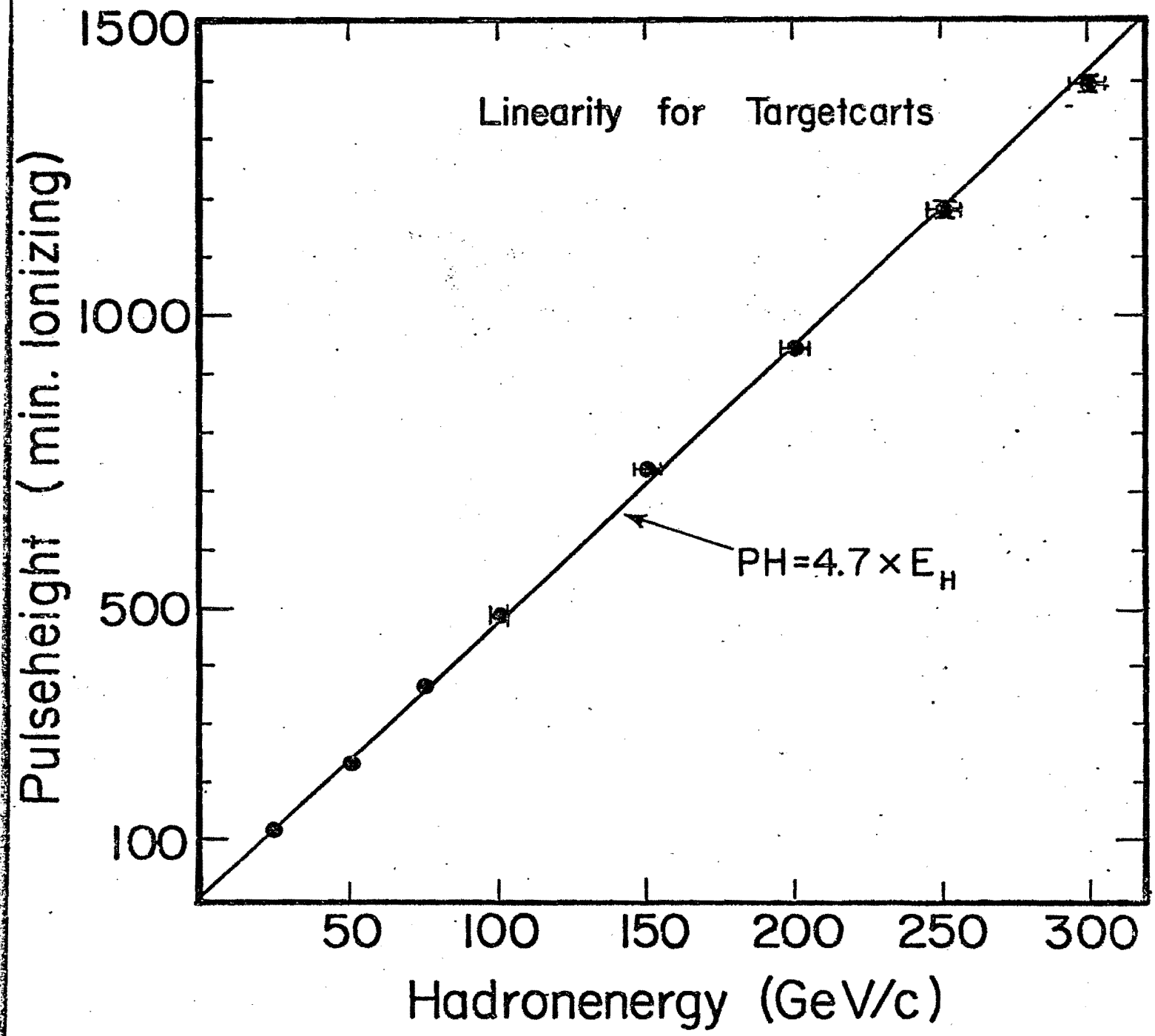

Figure D3

Linearity curve: Pulse height versus hadron shower energy.

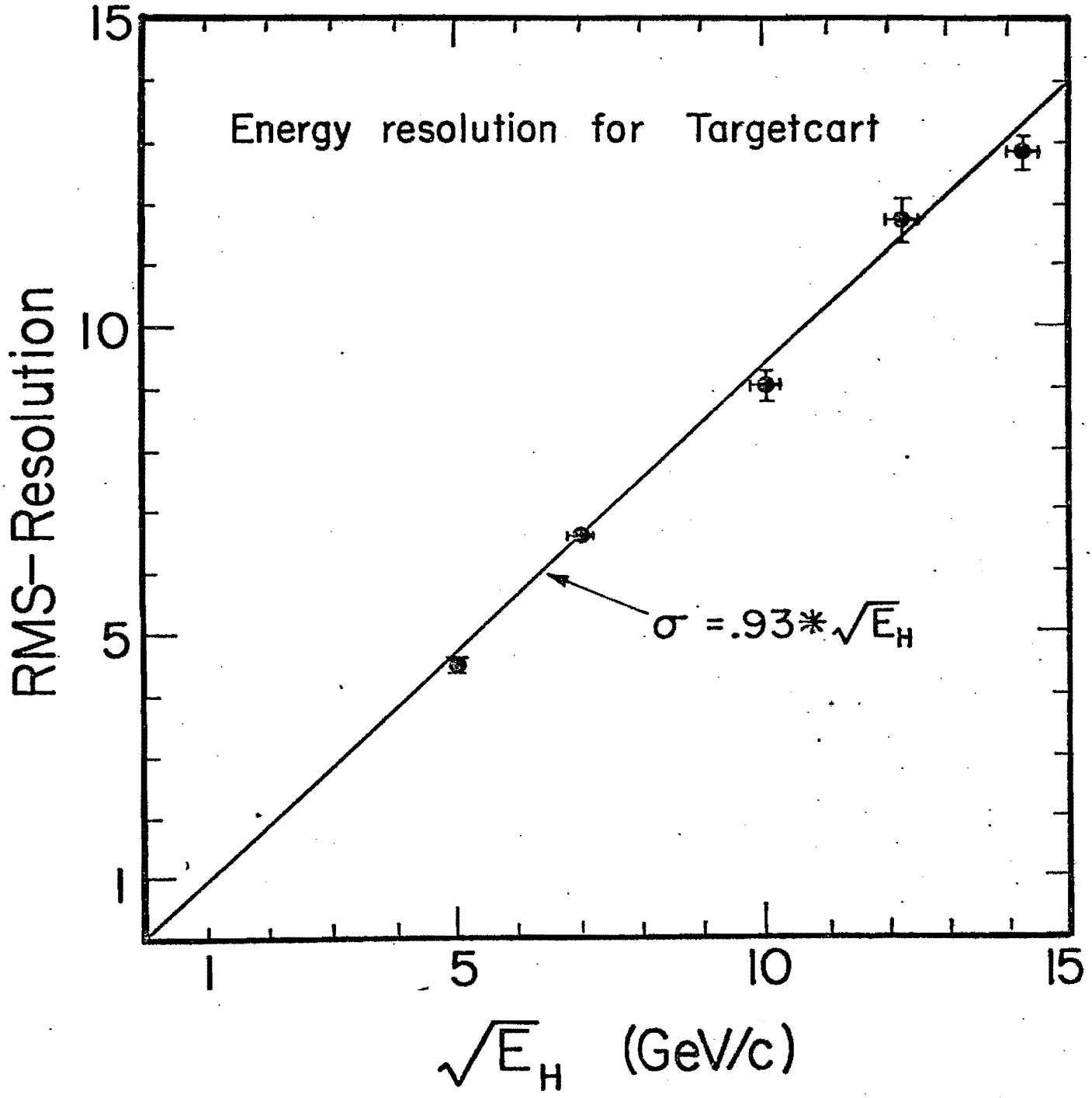

Figure D4

Energy resolution for hadron showers.

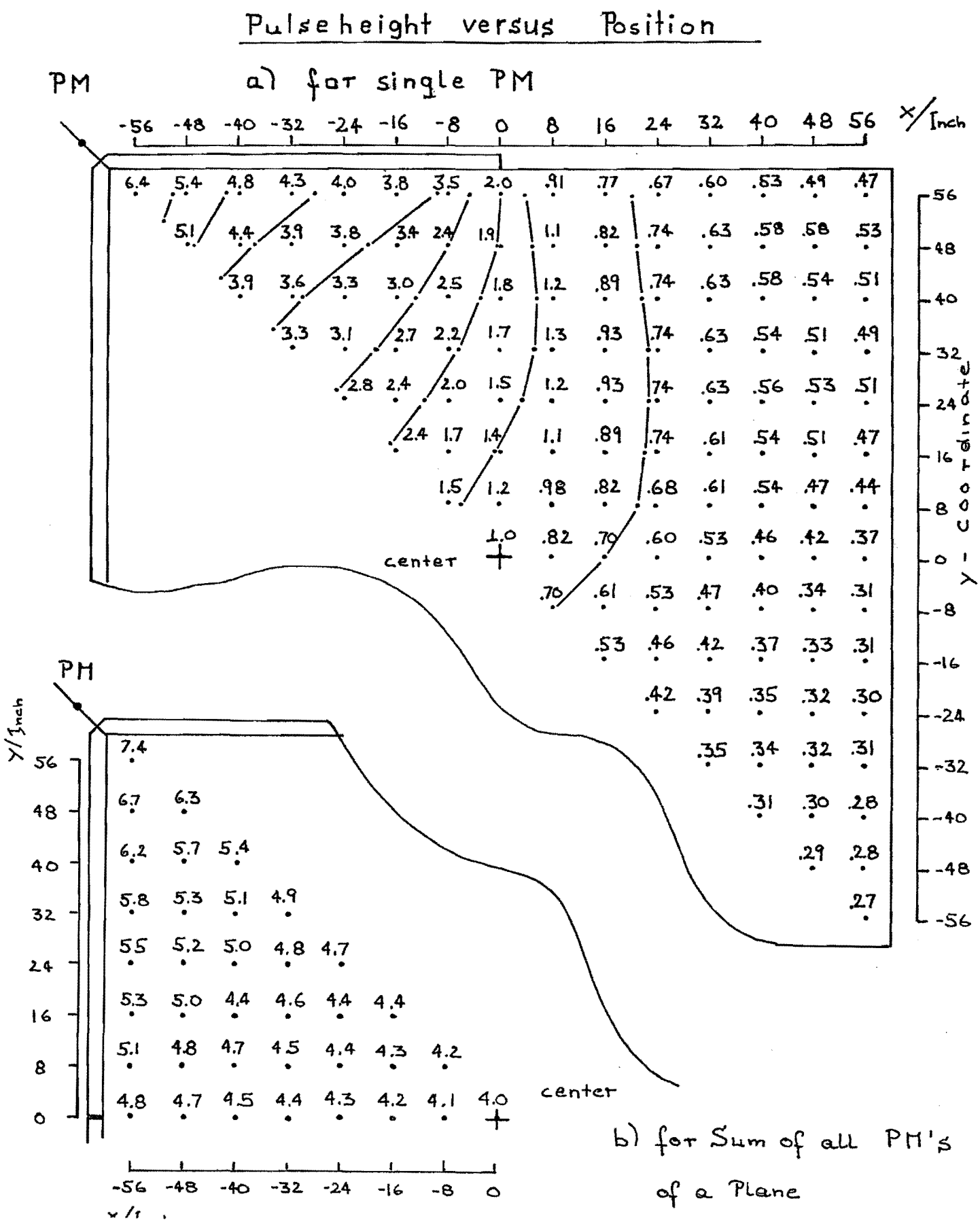

Figure D5

Variation of pulse height with position.

When all the corrections are made, the hadron energy, determined by these counters, and the muon energy, determined by the toroid spectrometer system, are combined to give the observed neutrino energy. Since 98% of the neutrino flux is due to two-body decays, the neutrino energy can be inferred from the initial hadron decay angle, which in turn, is determined by the beam geometry and the radial displacement of the event from the beam axis. This energy is, of course, subject to the two-fold ambiguity of the neutrino parent. However, the favorable geometry of the Fermilab dichromatic neutrino beam combined with the good resolution of the Lab E apparatus give the precision to make an unambiguous choice as to the initial ν energy. Figure D6 shows preliminary results on the mean observed total energy versus radius for events obtained during the initial run of E356 with the beam tuned to 300 GeV. The solid lines are a Monte Carlo calculation of the energy spectrum for the dichromatic beam using realistic beam divergences and spot sizes. The points are obtained from the measured events. The horizontal error bars show the width of the bins chosen; the vertical error bars are set at 5% although the statistical errors are smaller. There has been <u>no</u> shifting of energy in either the calculation of the beam energy or in the calibration of the hadron calorimeter or muon spectrometer. This graph confirms the absolute calibration of our measurements and clearly demonstrates the dichromatic nature of the beam. The deviation of measured values from calculated values at large radii, for the pion neutrinos, is due to wide-band background at low energy. This background is related to difficulties in dumping the proton beam at high positive tunes and should be corrected for our next run.

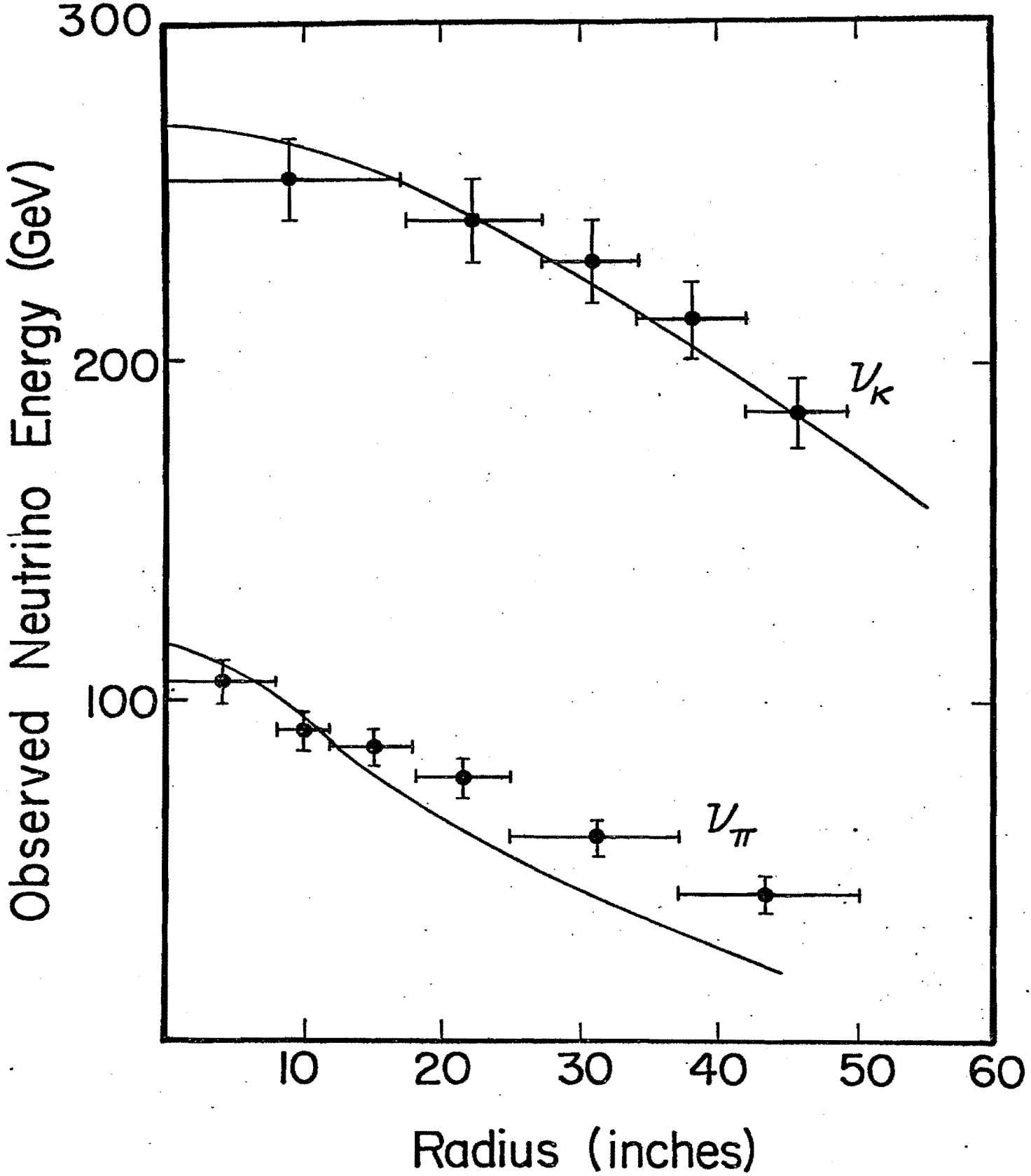

Figure D6

Observed neutrino energy versus Radius

REFERENCES

D1 B. C. Barish et al., Very Large Area Scintillation Counters for Hadron Calorimetery.
IEEE Transactions on Nuclear Science NS-25 (1978) 532.

Appendix E: Comparison of this experiment with its European Counterpart

In proposing this experiment, we are vaguely aware of a comparable experimental apparatus presently operating on the mainland of Europe. It is inevitable that the question will pose itself as to the relative strengths and weaknesses of the two devices for doing the physics described in this proposal. Though such questions contain a certain inherent tackiness, we anticipate them and shall attempt to respond with our customary restraint, humility, and objectivity. Table E1 shows a comparison of the general features of the two set-ups.

The total mass(item 1) of the two set-ups are similar. The Lab E modules have built-in capabilities for horizontal rearrangement. (Note that some vertical rearrangement has occurred in the Alpine device to partially compensate the Emmentaler effect (see below).) A detailed comparison of the calorimeters(item 2) shows that the Lab E set-up has a more massive fine resolution section. This section is also uniform and un-magnetized, without the very serious complications arising from the hole and coils(Emmentaler effect) in the Swiss target calorimeters, which double as toroids. It should be noted that the Fermilab target has twice the steel thickness(10 cm) between scintillation counters of its counterpart(5 cm), a major factor in total cost, and yet has an almost identical experimentally established energy resolution.

The CERN apparatus has a larger crude sampling calorimeter; however, when the fiducial cuts are made[8] the actual usable target volume is not appreciably larger than the Fermilab apparatus.

The obvious advantage of choosing a totally magnetized calorimeter system (European Plan) over the separated function target-calorimeter and muon spectrometer(American Plan) is that of acceptance, particularly at large x and y. Figure E1 shows the calculated acceptance of the fine target portion of the Fermilab apparatus at various x-values. Note that at the typical mean

Table E1: Comparison of this Experimental Apparatus with its European Counterpart

	CFRR	CDHS
1.	Weight Movable = 1100 tons	Weight Fixed = 1380 tons
2.	Calorimeter Instrumentation	
	680 tons: 10 cm spacing, Uniform Calorimeter, $\Delta E/E = 0.93/\sqrt{E}$	510 tons: 5 cm spacing, 30 cm hole on axis, $\Delta E/E \sim .9/\sqrt{E}$
	420 tons: 20 cm spacing, 25 cm hole on axis, $\Delta E/E \approx 2/\sqrt{E}$	580 tons: 15 cm spacing, 30 cm hole on axis, $\Delta E/E \sim 1.8/\sqrt{E}$
		290 tons: Uninstrumented
3.	Position Detection	
	Spark Chambers	Drift Chambers
	Every 20 cm of steel	Every 75 cm of steel
	Uniform target	30 cm hole on axis
	Not magnetized	Magnetized
	Recognize spark $\geq$ 1 chamber from vertex (ie after 20 cm)	Recognize spark $\geq$ 2 chambers from vertex (ie after 150 cm Fe)
	$\Delta\theta_\mu \simeq 0.1/p_\mu$	$\Delta\theta_\mu \sim 0.3/p_\mu$
	$\Delta p/p \approx 10\%$	$\Delta p/p \approx 9\%$
4.	PR poor	PR excellent

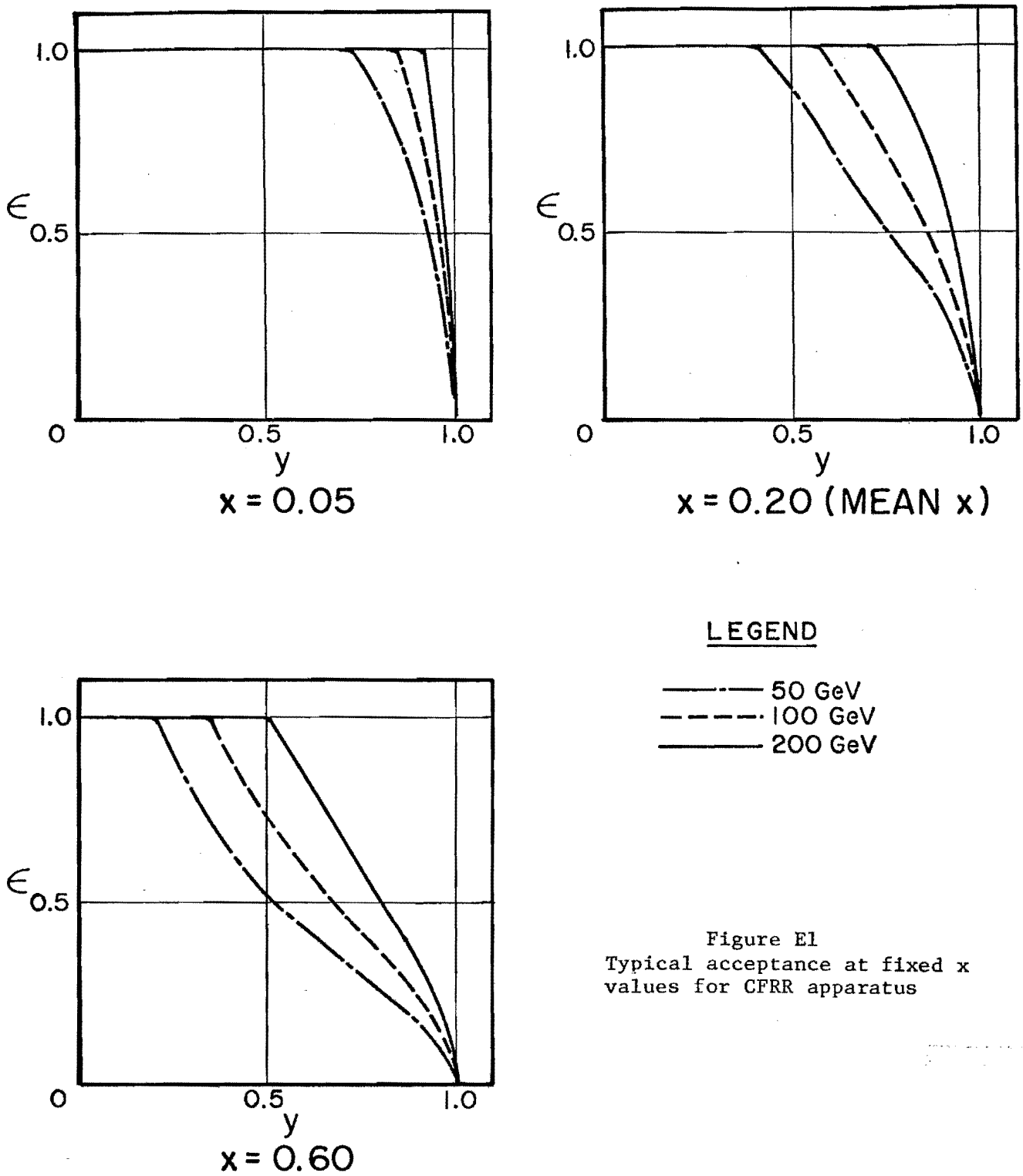

Figure E1
Typical acceptance at fixed x values for CFRR apparatus

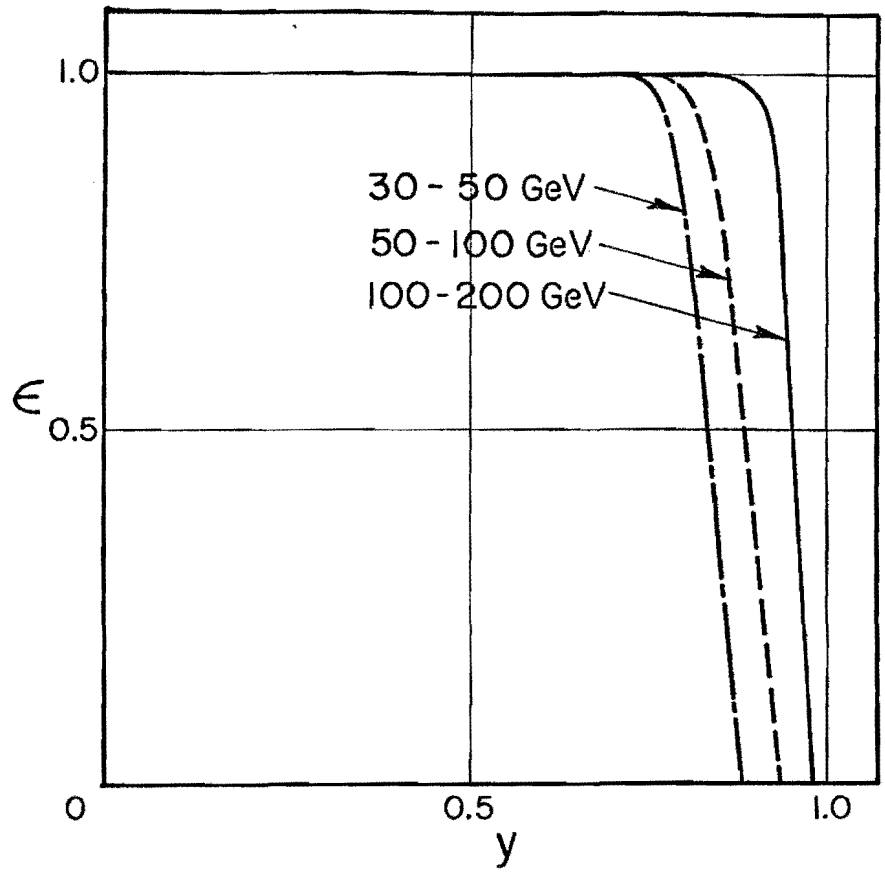

Figure E2
CDHS acceptance

value of x = 0.2, the acceptance compares favorably with the published average acceptance of the CDHS apparatus, shown in Figure E2. The acceptance of the Fermilab system is very large at small values of x where the predicted value of R is expected to be quite large. (Note also that as E_ν becomes large, the differences become even smaller.) This comparison has not assumed use of the muon spectrometer portion of the Fermilab set-up as target, which would boost the event rate at large y. Since large y corresponds to large E_ν and small E_μ, this region will provide events with little compromise in resolution.

For this proposed experiment, the smaller acceptance at large x of the Fermilab apparatus will not be very important, unless it turns out that R is large in this region(see Figure 1 for prediction). If this happens to be the case, the apparatus can be trivially reconfigured to substantially boost the acceptance at very large x, by translating the toroids transversely with respect to the target. The modular and flexible nature of the Lab E set-up allows response to such physics problems with minimal cost and difficulty.

In position detection(item 3), different choices were made on the technology to apply and on the spacing of the detectors. Our choices were motivated in part to provide better angular resolution by more than a factor of 3(see below). The Fermilab apparatus utilizes magnetostrictive spark chambers located every 20 cm of steel; the CERN apparatus incorporates drift chambers placed every 75 cm of steel. The magnetostrictive chambers are limited to one event per fast spill; however, the requested mode of operation for the dichromatic beam is to have multiple fast spills with the intensity chosen to be consistent with the trigger rate. The magnetostrictive chambers can easily run for multiple events on slow spill, but this mode of operation will increase the cosmic ray background and eliminate the possibility of studying neutral currents. The CERN drift chambers have the possibility of handling multiple events in a single fast pulse. This capacity is primarily useful

for the wide band horn neutrino beam running and is not as important in the dichromatic neutrino beam mode where the trigger rate is typically 1 event/10^{13} protons.

The operation of the magnetostrictive target chambers has been superb. The chambers have extremely good multi-spark capability, and permit the muon to be tracked back to the vertex in a large number of cases(see Appendix C). This, combined with other factors, is very important in the accurate determination of muon angles.

The other major considerations in measuring muon angle are (1) the use of an unmagnetized target so that the angle can be determined with as few as three position coordinates near the vertex, and (2) more frequent position sampling, so that less steel is traversed before angles are measured. Figure E3 shows a calculation of the projected-angle resolution(rms) in our experiment with 40 cm spacing(containing 20 cm steel) between chambers versus inverse momentum. The calculation includes a correct treatment of multiple scattering for the angle determination. The curves for the observed track in the first (n_s=1) or the second (n_s=2) chamber downstream of the vertex are shown. For comparison, we show typical curves for an apparatus with 103 cm spacing(60 cm steel) magnetized target. The difference in angular resolution is of order a factor of 3.

The muon angle resolution is the determining factor in x resolution at small x (see Section VII and Figure 10). For example, for E_h= 25 GeV, σ_x= 0.015 at x = 0.05 with our resolutions. Clearly, a factor of 3 worse precision in the angle determination would create problems in this region. For large values of R at small x(see Figure 1), this resolution directly affects the physics of this proposal. Another physics question related to angle resolution is the Gross-Llewellyn-Smith sum rule:

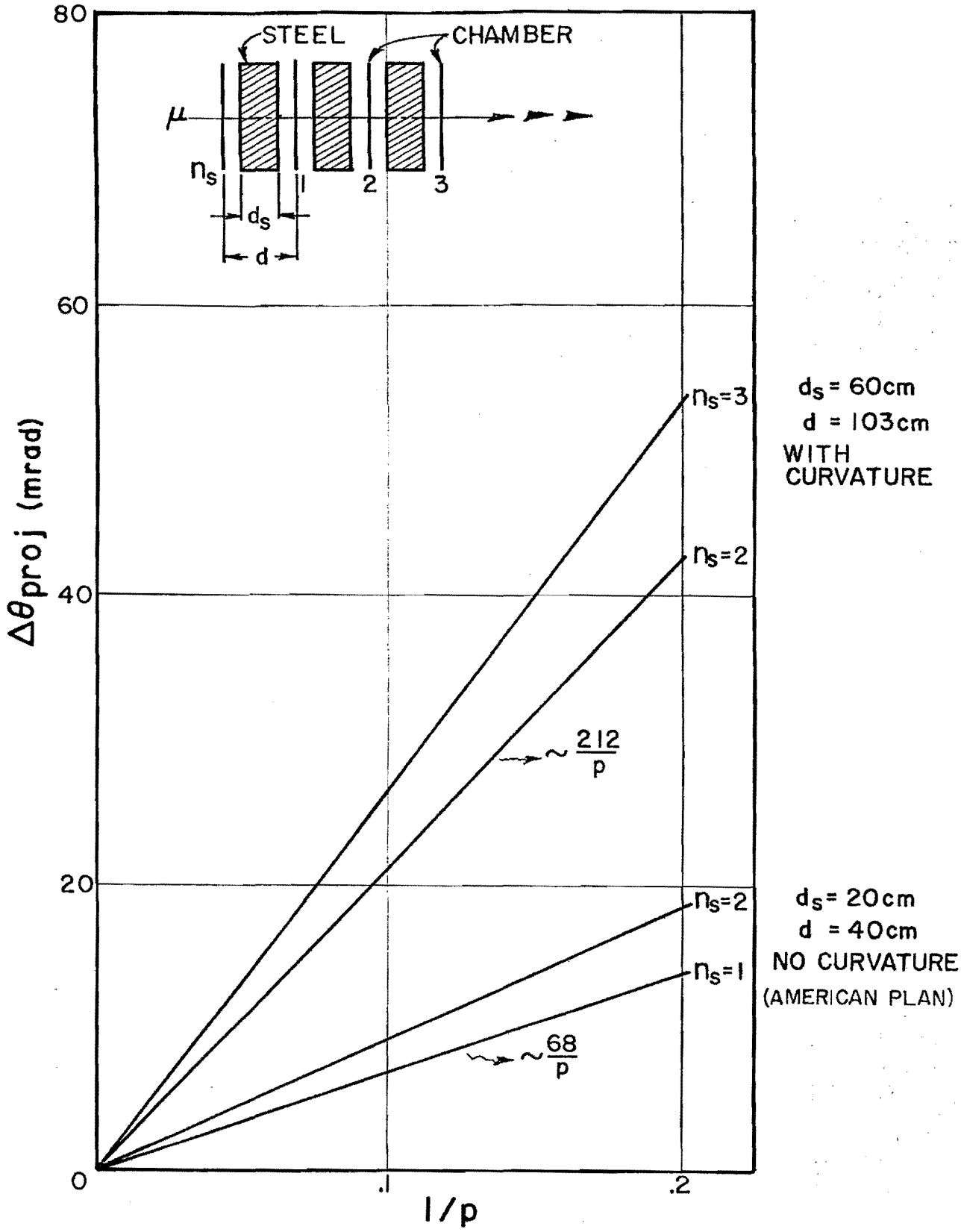

Figure E3
Angular resolution with two different approaches to position detection

$$\lim_{x_{im} \to o} \int_{x_{min}}^{1} \frac{xF_3}{x} \, dx = 3$$

which requires x_{min} as small as possible. This experimental test obviously requires good x-measurements at small x. At small x, the resolution is given by

$$\Delta x = \Delta\theta \sqrt{\frac{2E}{M} \frac{1-y}{y}} \sqrt{x}$$

Below some critical x value, x_c, the error becomes larger than the x-value ($\Delta x \simeq x$ at $x = x_c$), and clearly

$$x_c \; \alpha \; (\Delta\theta)^2$$

It makes little sense to take x_{min} smaller than x_c . Hence, a factor of 3 improvement in angular resolution is worth an order-of-magnitude in the lower limit of the x-integration for checking this important sum rule.

The overall impression which one receives from these comparisons is one of equality with slight differences in emphasis relating to certain physics topics. For the physics of this proposal the Fermilab apparatus has some major advantages; namely, a larger high resolution target and greater precision on measurements of x.

We conclude with a parting comment on item(4) of Table E1 which is a clear difficulty given the necessity of this appendix. It is to be hoped that this proposal contains some factual information rectifying this situation. If this proposal is not approved, we have clearly not succeeded in turning this situation around. In that event, it will be important to open lines of communication with groups more talented in this regard and to find applications which will provide good use for the existing apparatus. (One line of thought is in studying communication via neutrino beams, a group which has recently demonstrated great talent as regards to item 4.)